MECHANICS OF COHESIVE-FRICTIONAL MATERIALS, VOL. 2, 121–163 (1997)

Experimental micromechanical analysis of a 2D granular material: relation between structure evolution and loading path

F. Calvetti[1], G. Combe[2] and J. Lanier[2]

[1]*Politecnico di Milano, Milano, Italy*

[2]*Université J. Fourier, Grenoble, Laboratoire 3S-IMG, B.P.53, 38041 Grenoble, France*

SUMMARY

This paper is concerned with micromechanics of Schneebeli material specimens composed of wooden roller stacks. Several laboratory tests are carried out to analyse the material behaviour under complex loading conditions, involving loading–unloading cycles and principal axes rotations. In order to characterize micromechanical deformation features and structure evolution, a series of pictures is taken during loading. Pictures are then digitized using a stereo device, obtaining the position of each roller. Starting from these data a number of computer programs, conceived for the purpose, allow us to measure micromechanical variables and to analyse their evolution.

In the following, after the description of the devices employed in this research, macromechanical results are analysed to evaluate the reliability of the laboratory model. Then, local variables are introduced and the use of continuum mechanics to describe granular materials behaviour is discussed. Finally, the evolution of local kinematic variables is described, focusing interest on the evolution of specimen anisotropy. © 1997 by John Wiley & Sons, Ltd. Mech. cohesive-frictional mater. 2, 121–163 (1997)

KEY WORDS: granular materials; micromechanics; biaxial tests; complex loading paths; micro–macro relations; fabric anisotropy

1. INTRODUCTION

Granular materials, like sand or gravel, are composed of distinct particles interacting at contact points. Within such materials, the contact network provides internal transmission of forces, whose averaging over a sufficiently wide volume allows us to define a continuum-equivalent stress tensor. On the other hand, local kinematics is described by translational and spin velocity of particles: the non-uniform distribution of these variables gives rise to macroscopic deformations. Local behaviour is ruled by simple principles: contact shear force cannot overcome a threshold fixed by Coulomb's law, and contacts are only active in compression. These two limitations represent the main source of weakness of granular materials; moreover, they can be considered as responsible for the complex macrobehaviour of sands, since they allow important structure changes during loading. Nevertheless, on a global scale, granular materials are usually considered as continua, neglecting their discrete nature; as a consequence, constitutive models are based on macromechanical observations, and granular materials can therefore be treated in the framework of elastoplasticity. Probably owing to the scale of approach, such models either are unable to reproduce real sand behaviour under complex load histories or need the introduction of several internal parameters, like plastic deformation and hardening variables, whose physical meaning is generally not clearly defined.

CCC 1082–5010/97/020121–43 $17.50

Received 20 March 1996
Revised 8 October 1996

In recent years, increasing interest has been focused on micro–macro mechanical approaches, with the fundamental aim to deduce the behaviour of the equivalent continuum from micromechanical considerations.

First of all, a theoretical approach is necessary to define macroscopic quantities, such as stress and strain tensors from local variables (microscale). The stress tensor is generally obtained by discrete averaging of interparticle forces, either on the boundary of an elementary representative volume (ERV), or on the whole volume[1––6]. These different definitions may lead to a symmetric or non-symmetric stress tensor. Caillerie[7] has shown that the anti-symmetric part is or order a/L where a is the grain size and L the ERV size. As a consequence this anti-symmetric part may be generally neglected at the macro scale. The definition of deformation is more difficult: one can consider the displacement field u_i at the boundary of the ERV and, using divergence formula, an average gradient $\bar{u}_{i,j}$ is defined.[2,3] Another way may be the use of equation of internal work.[9] In this case the relative displacement of contact points in the whole ERV is introduced. This point will be discussed in Section 4.3.

Then, an homogenization process can take place, in three steps:

1. Definition of loading condition at the boundary of the ERV.
2. Localization operation, which means resolution of the boundary problem in the ERV (at the micro scale). This operation needs the definition of contact rules between grains.
3. Homogenization of the micromechanical response which gives the macroscopic constitutive relation (relation between stress and deformation).

This theoretical scheme presents a major difficulty (point 2) because the geometry of the structure is not *a priori* known. To overcome this problem Cambou *et al.*[10] proposed to follow the same scheme but with averaging quantities. In our opinion this is the main difficulty with a granular medium: how to describe, in a representative way, its structure and its evolution? Many attempts were proposed with the so-called fabric tensor.[11,12] This point is discussed in Section 5.

Numerical approaches, known as the distinct element method (DEM), give interesting solutions for point 2 (localization). Cundall was a pioneer researcher in this field. The main idea is to consider mechanical evolution of the structure as a dynamic process. Newton's law is applied for each grain and results of the calculus are velocities, displacements and forces acting on the grains. Very interesting results are obtained by this way.[2,13–18] The general trends of macroscopic behaviour such as irreversibility, limit strength and induced anisotropy are well reproduced. Quantitative agreements with analogue laboratory tests are not yet completely tested essentially because the experimental and numerical preparations of the sample are not exactly the same. It is worth mentioning the results obtained with PFC^{2D} code by Bornarel[19] who took the initial configuration from a laboratory specimen tested with our shear device. In this case, very good quantitative agreement was obtained.

The last approach is an experimental one, to see what really happens in granular materials when macroscopic deformations are imposed. Such researches are useful to physically understand the behaviour of such materials and also to validate numerical models. The full description of micromechanical behaviour may be divided into three points:

1. Description of the structure, that is to say, position of grains and contacts between them.
2. Description of the kinematics evolution: displacements, rotations, evolution of contacts.
3. Description of intergranular forces.

Experimentally, 2D materials (Schneebeli rods) are generally used for simplicity. The first two points need the ability to digitize the position of grains at each step of the macroscopic deformation.[20,21] The third point is more difficult because measurement of forces needs sophisticated techniques such as photoelasticity.[1,22–24]

In this paper, experimental results are presented concerned with micromechanical behaviour of granular materials. The tests are performed on a special shear apparatus. The whole experimental procedure is described in the first part. Then, analysis of displacements, rotations and contact evolution is presented for different loading paths: biaxial compression, simple shear, and complex paths with controlled rotation of principal axes. As far as possible, links with continuum mechanics predictions are proposed.

2. EXPERIMENTAL PROCEDURE

Tests presented here were performed at Laboratoire 3S in Grenoble, by means of a biaxial shear apparatus named $1\gamma 2\varepsilon$. This machine allows a specimen composed of a roller stack to be subjected to most general 2D-loading conditions, independently applying deformation along vertical and horizontal axes, and shear.

2.1. Material description

The granular material which was used in the following tests is an assembly of smooth wooden rollers with three diameters ($\Phi = 13$, 18, 28 mm) and 6 cm long. The intergranular friction angle is about 28° ($\pm 2^\circ$) (see Appendix A for the experimental measure). The total number of rods which are needed for filling the testing frame is about 750, but generally only 300 rods, in the central part of the specimen, are observed (100 of each diameter) (Figure 1).

2.2. Testing apparatus

Tests are performed with a special shear apparatus described in Joer *et al.*[25] This apparatus is essentially a deformable parallelogram with five electric motors which impose the deformation: four motors, synchronized two by two, control the lengths L_1 and L_2, the fifth motor controls the distortion γ (Figure 2). In fact, each side is realized with five trolleys which travel on a track and allow us to split the change of length ΔL in five equal parts and make boundary conditions close to homogeneous deformation. For tests with shear load, shear stress transmission at the plates is granted by fixing small aluminium rods (diameter 3 mm) to the trolleys.

2.3. Measurements

Plates lengths, $L_1(t)$ and $L_2(t)$, and the distortion, $\gamma(t)$, are measured with five potentiometers. Macrostrains and the rigid rotation of the specimen may be deduced in the following way:

$$\varepsilon_x = \frac{\Delta L_1(t)}{L_1(t_0)}, \varepsilon_y = \frac{\Delta L_2(t)}{L_2(t_0)}, \varepsilon_{xy} = -\omega_{xy} = \frac{1}{2}\gamma(t)$$

Three corners, O, A and B (Figure 2), are equipped with strain gauged hinges which allow measurements of the two components, F_x and F_y, of forces acting between the two faces linked at these points. Writing down the equilibrium of faces OA and AB we can deduce F_n and T, normal and tangential actions of the material on these faces. Assuming homogeneous state of stress, the corresponding normal and tangential stresses σ_n and τ are obtained, from which the macroscopic state of stress (σ_x, σ_y, τ_{xy}) is deduced.

2.4. Test control

The control of this apparatus is obtained by imposing motor velocities and as a consequence load histories are basically strain-controlled. Any strain path $\varepsilon_x(t)\varepsilon_y(t)$, $\gamma(t)$ may be easily performed. Stress

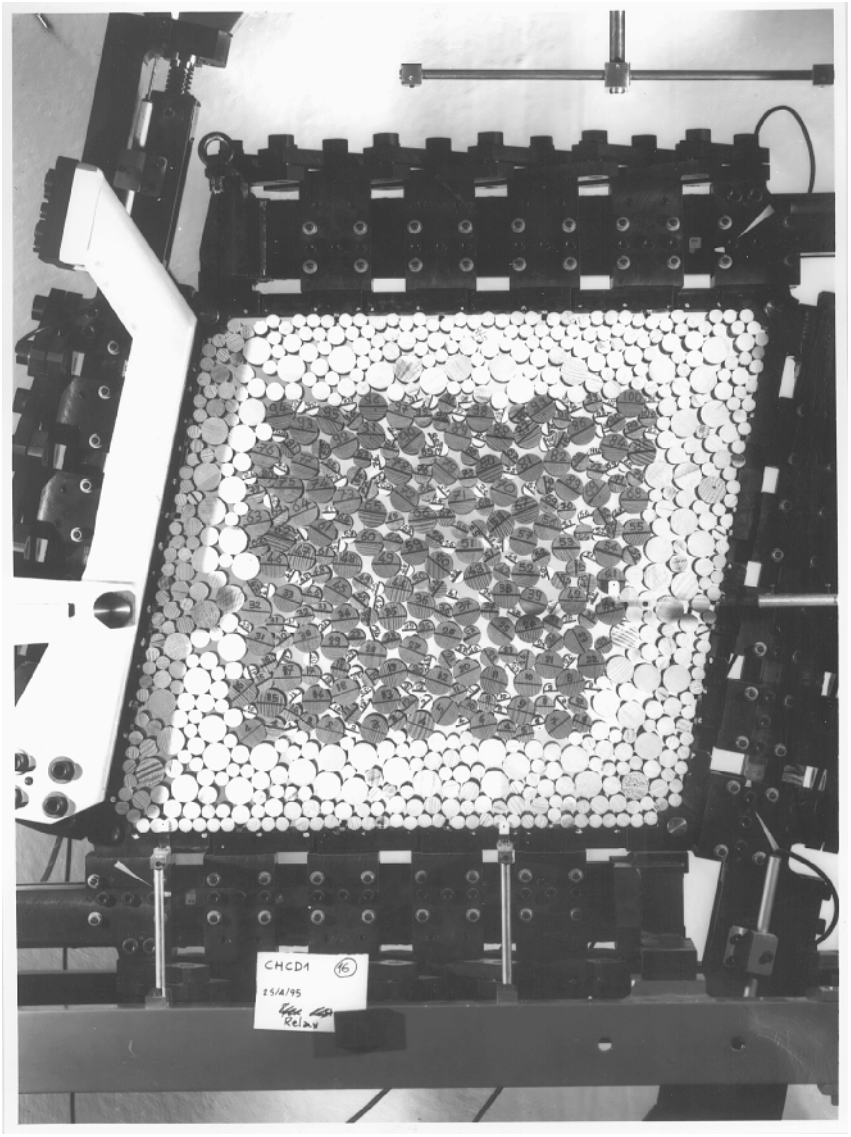

Figure 1. Picture of the loading device during shear test

control is obtained by use of servo-control: any component of the stress state, σ_x, σ_y or τ_{xy}, is kept close to the imposed value acting on $\varepsilon_x, \varepsilon_y$ or γ respectively. In this way, any strain or stress-controlled test may be achieved.

2.5. Micromechanical measurements

In order to characterize displacements and rotations of rollers, a series of pictures of the specimen is taken during loading (Figure 1, Figure 3(a)). On picture negatives (9×10 cm) five fixed points define the laboratory frame; rods are numbered ($k = 1, N$) and an orientated diameter $(AB)_k$ is drawn on each of them (Figure 3(b)). Diameter ends and fixed points are digitized with a stereocomparator

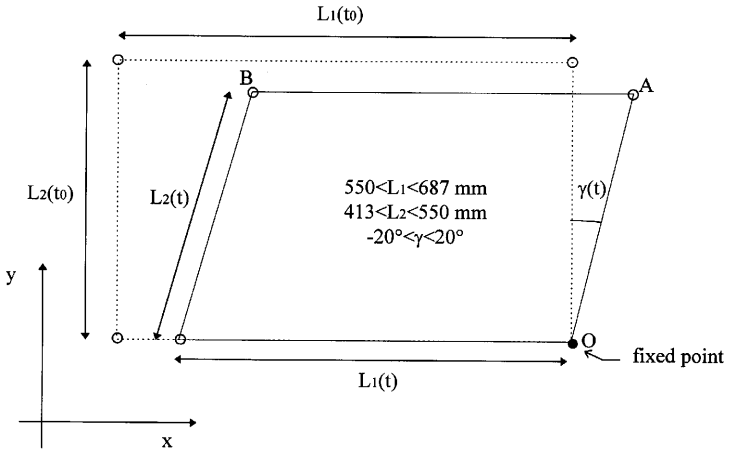

Figure 2. Principle of the shear apparatus '1γ2ε'

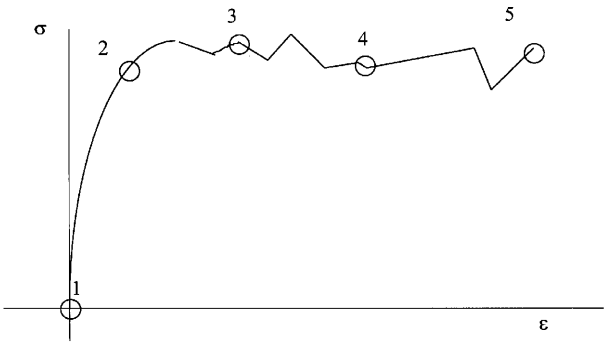

a)

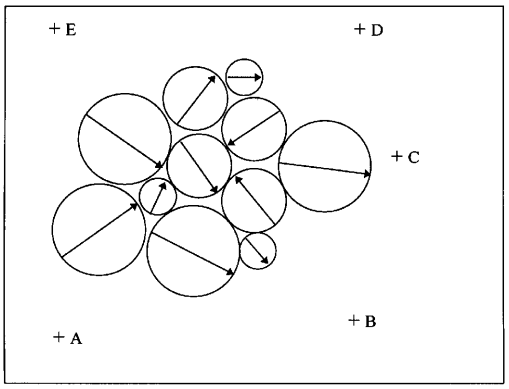

b)

Figure 3. Micromechanical measurements: (a) localization of pictures on the loading path; (b) schematic picture with rods and fixed points to define laboratory frame

(DSR 15—Leica). Measurement precision is about 5μm on the negative for well defined points, which corresponds to $5/100$ mm in the real laboratory scale, but precision is not so good for diameter ends.

A number of specific computer programs are written to analyse these data. First, the position (x_k, y_k) of the particle centre and the measured radius R_k are defined. Contacts are detected with a tolerance of 0.5 mm. Secondly, by comparison of two pictures, displacements, rotations and changes in the contact network may be defined.

3. TESTS AND MACROSCOPIC RESULTS

As we deal with an analogous material, strains and stresses measured at the specimen boundaries, i.e., macroscopic results, must be compared with those obtained on similar laboratory tests performed on real sand specimens. A qualitative agreement is required to validate the 2D-model and to extend micromechanical observations to the modelling of actual granular materials. For this reason, before gaining insight into the microworld, we will describe the macrofeatures of tests and the boundary behaviour of the specimens. From a macromechanical standpoint, tests can be divided into two main categories: tests without rotation of principal axes of stress and strain; and tests with principal axes rotation. Every test is labelled with a name describing load history: as we will often refer to tests using the corresponding label, we will first detail the meaning of letters forming test names: V stands for *vertical compression*; H stands for *horizontal compression*; D and G stand for *right shear* and *left shear* respectively (cisaillement à *droite* et à *gauche*, in French); C is used for tests with *constant normal stress*; and U is used for *constant volume* tests. For instance, CHCD1 is a test in which the specimen is first loaded in horizontal compression (H) ($\dot{\varepsilon}_x = \text{constant}$) under constant vertical stress (C), and then subjected to right shear (D) ($\dot{\gamma} = \text{constant} > 0$) under constant vertical stress (C).

All tests are preceded by an isotropic compression, up to a confining pressure of 50 kPa.

3.1. Specimen preparation

At the beginning of each test, the specimen was hand built placing each roller until the device frame was filled-up. This operation is a crucial one if we wish specimens to be initially homogeneous and isotropic; this means that different sized rollers must be uniformally distributed and preferred orientations in contacts must be avoided. In fact, when a roller is placed in the vertical device frame, vertical contacts are unstable and the roller is likely to fall in the hollow between two lower rollers. As a result, the specimen fabric risks being characterized by a lack of vertical contacts, and many contacts are found to fall around the directions corresponding to triangular cells, which represent the densest fabric for equal-sized rollers. This point will be discussed in Section 5.1. A consequence of the described procedure is that it was not possible to create loose specimens. Moreover, to obtain an adequate load diffusion at specimen boundaries, a layer of small rollers (diameter 13 mm) was placed along device plates (see Figure 1).

3.2. Tests without axes rotation

This group includes three compression tests and a shear test under constant volume conditions (Table I). During these tests the principal directions of strain and stress tensors are fixed and coincide. Nevertheless, sudden permutations between major and minor principal directions take place when the load is reversed. Results obtained from this series of tests can be qualitatively compared with results of triaxial tests on real sand specimens. From a micromechanical point of view, tests without axes rotation were particularly useful to study micromechanical deformation features and the development of fabric anisotropy.

Table I. Tests without rotation of principal axes with schematic strain paths

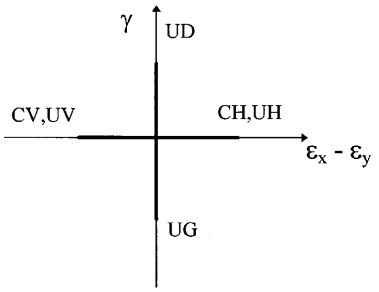

Test type	Test label	Macroscopic boundary conditions (control)
Compression tests	CVCH1	part CV: $\sigma_x = 50$ kPa; $\gamma = 0$; $\Delta\varepsilon_y > 0$ (loading); $\Delta\varepsilon_y < 0$ (unloading) part CH: $\sigma_y = 50$ kPa; $\gamma = 0$; $\Delta\varepsilon_x > 0$ (loading)
	CHCV1	part CH: $\sigma_y = 50$ kPa; $\gamma = 0$; $\Delta\varepsilon_x > 0$ (loading); $\Delta\varepsilon_x < 0$ (unloading) part CV: $\sigma_x = 50$ kPa; $\gamma = 0$; $\Delta\varepsilon_y > 0$ (loading); $\Delta\varepsilon_y < 0$ (unloading)
	UVUH1	part UV: ε_x such that $\varepsilon_v = 0$; $\gamma = 0$; $\Delta\varepsilon_y > 0$ (loading); $\Delta\varepsilon_y < 0$ (unloading) part UH: ε_y such that $\varepsilon_v = 0$; $\gamma = 0$; $\Delta\varepsilon_x > 0$ (loading)
Shear test	UDUG1	part UD: $\varepsilon_x = 0$; ε_y such that $\varepsilon_v = 0$; $\Delta\gamma > 0$ (loading); $\Delta\gamma < 0$ (strain reverse) part UD: $\varepsilon_x = 0$; ε_y such that $\varepsilon_v = 0$; $\Delta\gamma < 0$ (loading); $\Delta\gamma > 0$ (strain reverse)

3.2.1. Compression tests CVCH1, CHCV1 and UVUH1. In compression tests, principal strain and stress axes are vertical (y-axis) and horizontal (x-axis). During CHCV1 test, the specimen is first loaded and unloaded in horizontal compression under constant vertical stress (part CH); then the specimen is loaded in vertical compression under constant horizontal stress (part CV). The two parts of the test are identical except for a rotation of 90° of the major principal stress direction. The relative stress–strain curves are presented in Figure 4. The corresponding mobilized friction angles are similar: 33° in horizontal compression and 35° in vertical compression; but, the initial behaviour is quite different. The initial stiffness is higher for the first loading: the secant modulus corresponding to a deviatoric strain, ε_d, of 1% is about 11 MPa (first loading, CH part), to compare with 1.6 MPa (second loading, CV part). This drastic difference is related to anisotropy created by the first part of the test (see Section 5.2.1).

Another effect of former loading–unloading cycles may be observed on volumetric behaviour: for this purpose, we present results obtained during the CVCH1 test, which is similar to CHCV1, except for the order in which vertical and horizontal compressions are performed. During both vertical compression (pictures 1 to 4, Figure 5) and horizontal compression (pictures 5 to 10, Figure 5) the specimen volume initially decreases and then increases, but during the second compression the specimen is more compacting; on the contrary, dilatancy angle is not influenced by former loading. The same effects were described for real sand by several authors.[26–28]

Induced anisotropy influences in a similar way the material behaviour under constant volume conditions. During the UVUH1 test the specimen is first loaded in vertical compression, then unloaded and finally loaded in horizontal compression, as the volume is kept constant. As the test is fully strain-controlled, the specimen behaviour can be conveniently presented in the stress-path, plotted in the t–s' plane (Figure 6); t and s' can be respectively defined as:

$$t = \tfrac{1}{2}(\sigma_y - \sigma_x)$$

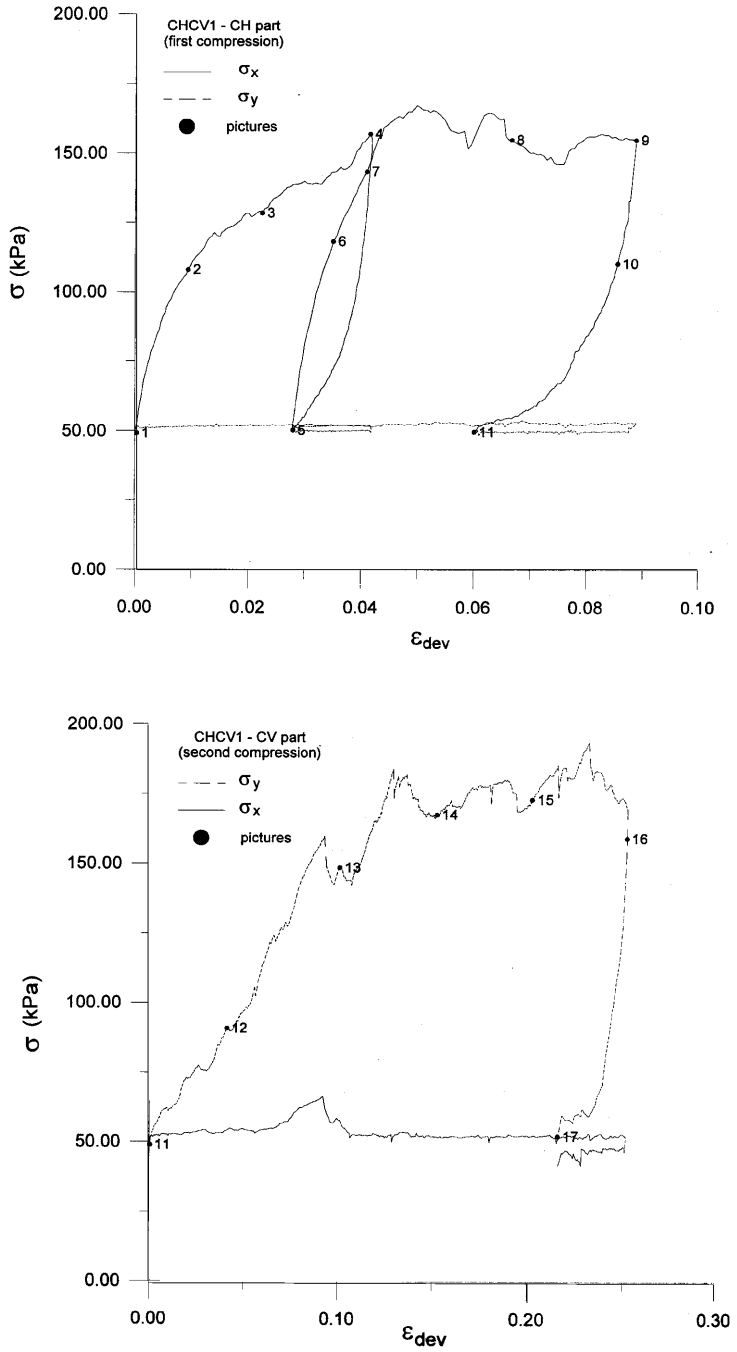

Figure 4. Test CHCV1, stress–strain curves: (top) horizontal compression; (bottom) vertical compression

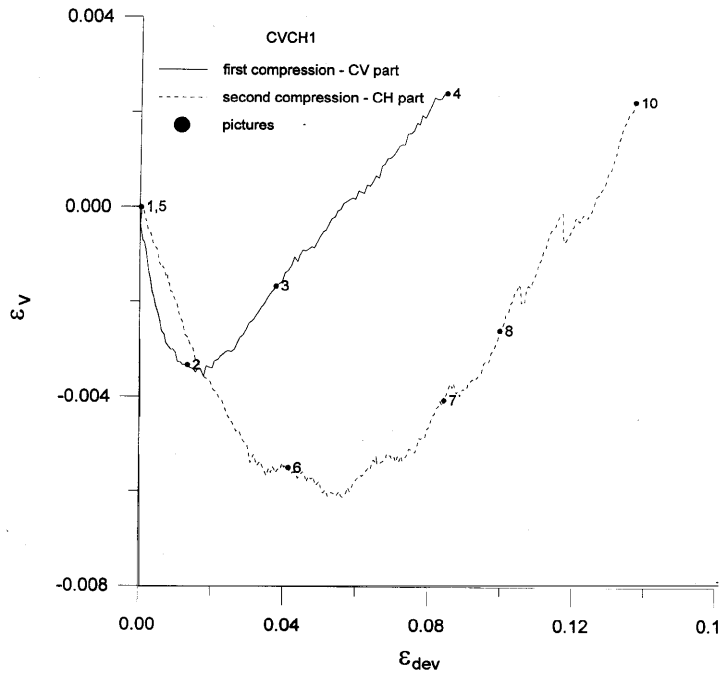

Figure 5. Test CVCH1: volumetric strain versus deviatoric strain during vertical and horizontal compressions

and

$$s' = \tfrac{1}{2}(\sigma_y + \sigma_x),$$

as σ_y and σ_x are principal stresses. In this case the mobilized friction angle is about 31° in both compressions. Nevertheless, during the first compression (UV part) the friction angle is rapidly fully mobilized, and the stress path reaches the limit-line without s' decrease. This behaviour can be observed only in very dense sands; on the contrary, during the second compression (UV part), the stress-path is similar to that which a medium dense sand would exhibit. As the test is performed under constant volume, and the density of the specimen is constant, the described difference is necessarily related to a different initial specimen structure: at the end of the first loading–unloading phase the contact distribution has a preferred orientation in the direction of the former compression, while a lack of contacts is found in the horizontal direction (see Section 5.2.1). From a macroscopic point of view, these considerations are confirmed if the stress-rate, which is closely related to the specimen stiffness, is analysed. For this purpose, we consider the distance between crosses traced on the stress path, which scan equal time intervals (Figure 6). The stress-rate is high at the beginning of compression, then slows and keeps constant as the stress path follows the limit line; the following unload phase is very rapid. When the load is reversed, the stress-rate dramatically slows down, while s' decreases. This means that the specimen is not able to carry loads in the reversed direction, while strains applied at the boundary are spent in structure rearrangement, i.e., to gain back a sufficient number of horizontal contacts. The point marked A in Figure 6 corresponds to the condition $\varepsilon_x = \varepsilon_y = 0$, which means that the specimen size is equal to the initial one. It seems interesting to note that after point A is reached, the stress rate increases, i.e., the specimen structure has sufficiently rearranged.

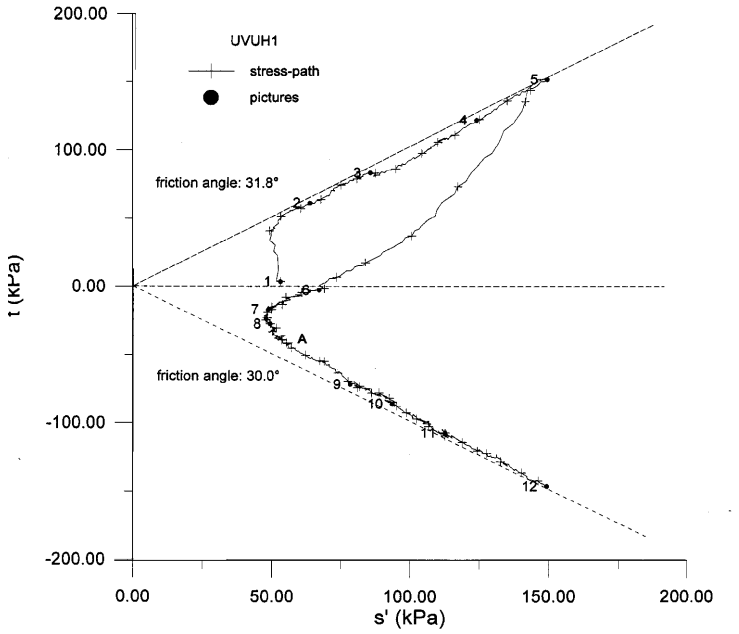

Figure 6. Test UVUH1: stress path

The presented results show that the macrobehaviour of the 2D material we employed is qualitatively similar to that a sand specimen would exhibit. Anyway, it is interesting to note that the volumetric behaviour of the specimen is a classical one for dense sands; on the other hand, the mobilized friction angle is close enough to the interparticle friction angle, which is likely to happen in loose sands. This qualitative difference is certainly due to the 2D nature of the specimens, but also to the roller shape, as was proven numerically by Rothenburg and Bathurst.[15] In fact, for given relative density and interparticle friction, the circular cross-section is the less adequate one to inhibit local failures in the form of particle slip and rotation.

3.2.2. Shear test UDUG1. UDUG1 is a shear test under constant volume conditions. Boundary strains are imposed controlling the rotation γ of the loading device lateral plates. This test is similar to compression test UVUH1, with the difference that stress and strain principal directions are 45° rotated from *x*–*y* axes. The specimen is subjected to two strain load–unload cycles, under right-shear (UD part) and left-shear (UG part) respectively. In Figure 7(top) we plot the stress-level

$$\eta = \frac{t}{s'} = \frac{(\sigma_I - \sigma_{II})}{(\sigma_I + \sigma_{II})}$$

versus the distortion angle γ. It is interesting to note that the stress-level curve has a certain symmetry with respect to the $\gamma = 0$ axis. If the stress-level is considered, three load phases are detected during the test (Figure 7(top)): the initial load under right-shear rate (pictures 1 to 5), the second one under left-shear rate (pictures 6 to 11) and the third one under right-shear rate again (pictures 12 to 14); the first load is far more rigid than the following ones, which are affected by former strain history (section 5.2.1).

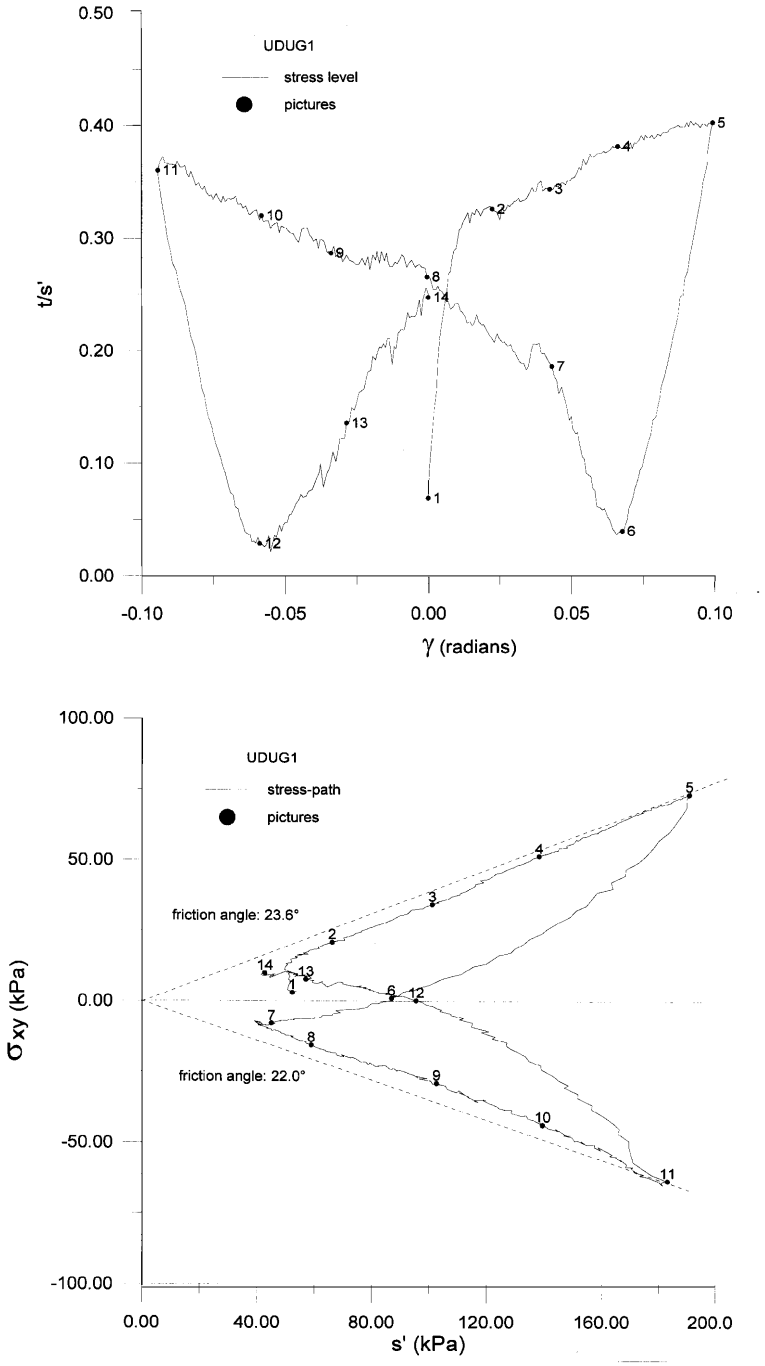

Figure 7. Test UDUG1: (top) stress level; (bottom) stress-path

As principal stress directions are fixed and 45° rotated from the *x*–*y* axes, σ_x is equal to σ_y and the stress-path lies on the plane

$$\frac{\sigma_x + \sigma_y}{2} \div \sigma_{xy}.$$

In this case, the stress path presents a well defined symmetry with respect to the $\sigma_{xy} = 0$ axis (Figure 7(bottom)). The qualitative behaviour is similar to that obtained during the UVUH1 test (Figure 6); anyway, it is necessary to note the fact that the mobilized friction angle is about 23°, far smaller than during compression tests: this difference is probably related to a bad shear-stress transmission at the device plates. Moreover, it is interesting to remember that Wood, Drescher and Budhu[29] using a simple shear apparatus have shown that during simple shear tests on sand the stress level measured at the plates is 10–15% lower in the middle of the specimen.

3.3. Tests with principal axes rotation

Another series of tests, in which sudden or continuous axes rotations were involved, allowed us to characterize a link within local fabric and macroscopic strain tensors. Two tests of this type were performed (Table II).

To visualize the principal strain axes rotation, the strain-path is plotted in the plane

$$\frac{\varepsilon_x - \varepsilon_y}{2} \div \frac{\gamma}{2},$$

which may be named *deviatoric 2D plane* (Figure 8). If *M* is a point in this plane, the corresponding polar angle is $2\alpha_{\text{epsilon}}$, where α_ε is the angle between principal strain axis and laboratory *x*-axis; in fact, the following relation applies:

$$\tan(2\alpha_\varepsilon) = \frac{\gamma}{\varepsilon_x - \varepsilon_y}.$$

In a similar way, if *M* and *N* are two points in this plane, the corresponding incremental strain, $\Delta\varepsilon$, is defined by vector *MN*, whose orientation is related with the orientation, $\alpha_{\Delta\varepsilon}$, of the incremental strain principal axes. If the two points are very close, the tangent to the strain-path at point $M = N$ gives the orientation, $\alpha_{\dot{\varepsilon}}$, of the strain-rate principal axes. In the following, we will use the terms *compression direction* and *compression rate direction* to indicate the directions defined by angles $\alpha_{\Delta\varepsilon}$ and $\alpha_{\dot{\varepsilon}}$ respectively.

The same considerations can be applied to stresses, if we use the deviatoric 2D plane

$$\frac{\sigma_x - \sigma_y}{2} \div \sigma_{xy}.$$

Table II. Tests with rotation of principal axes

Test type	Test label	Macroscopic boundary conditions (control)
Compression and shear	CHCD1	part CH: $\sigma_y = 50$ kPa; $\gamma = 0$; $\Delta\varepsilon_x > 0$ part CD: $\sigma_y = 50$ kPa; $\Delta\gamma > 0$; $\Delta\varepsilon_x = 0$
Principal axes continuous rotation	UR1	$\varepsilon_x = a\cos(\omega T)$; $\gamma = b\sin(\omega T)$; ε_y such that $\varepsilon_v = 0$

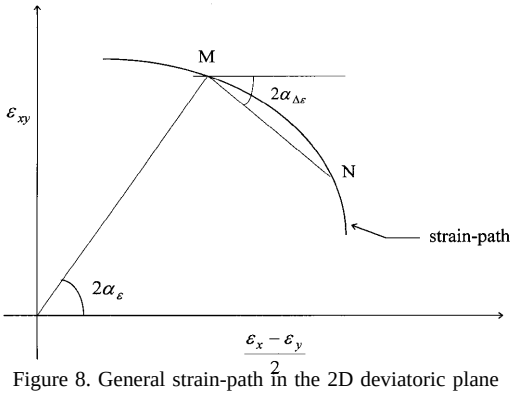

Figure 8. General strain-path in the 2D deviatoric plane

3.3.1. Test CHCD1: compression and shear. CHCD1 is a test in which, as vertical stress is kept constant, the specimen is first loaded in horizontal compression (CH part) and then subjected to right-shear (CD part). The corresponding strain-path is presented in Figure 9: during the first part of the test the direction of major principal strain, i.e., the compression direction, is horizontal; at the beginning of the CD part the incremental compression direction suddenly changes, and a rotation of the principal axes of stress and strain is produced. To give a synoptic view of the obtained results, the measured stresses (Figure 10(top)) and the volumetric deformation (Figure 10(bottom)) are plotted versus the deviatoric component of strain tensor, which is always increasing as the test goes on. The change in load conditions involves a rapid reduction of stress component σ_x, while the shear component σ_{xy} is quickly mobilized; after that, stresses keep almost constant as the specimen is

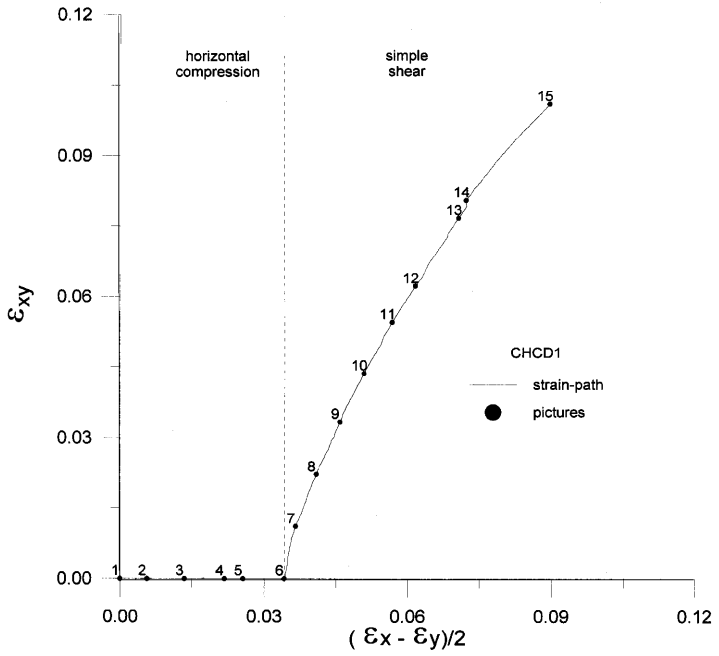

Figure 9. Test CHCD1: deviatoric strain-path

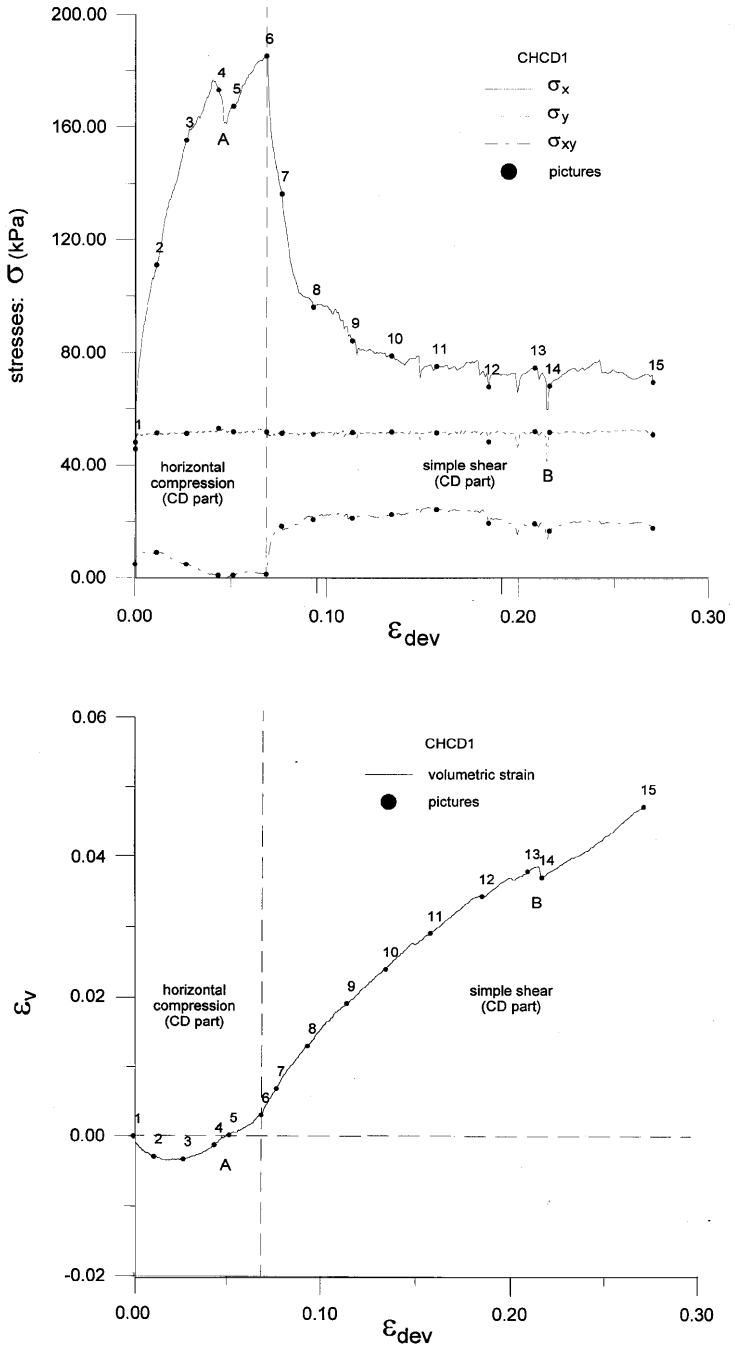

Figure 10. Test CHCH1: (top) stress–strain curves; (bottom) volumetric strain versus deviatoric strain

progressively sheared. The mobilized friction angle is larger during compression (35°) than during simple shear (24°), as obtained in tests without axes rotations.

Two points, labelled A and B on Figures 10(top) and (bottom), were experimentally characterized by local instability of rollers, in the form of sudden roller displacements, accompanied by dry noise emission. Corresponding to point A the stress curve shows a pre-peak; corresponding to point B the controlled stress component σ_y has a quick variation, and the specimen volume slightly decreases: this means that the specimen structure has a sudden collapse, as stress control is lost for a while. The micromechanical interpretation of the described behaviour will be detailed in the section regarding the internal specimen structure (see Section 5.2.2).

3.3.2. Test UR1: continuous rotation of principal axes. UR1 is a constant volume test in which shear and compression rate are trigonometric functions of time T, so that a continuous rotation of principal axes of strain and stress is obtained. The strain-path (Figure 11) is imposed in the form: $\dot{\varepsilon}_x = a \cdot \cos(\vartheta)$, $\dot{\varepsilon}_{xy} = b \cdot \sin(\vartheta)$, with $\vartheta = \omega T$; $\dot{\varepsilon}_y$ is determined by the constant volume condition. The actual strain-path does not come full circle, as we would like, because of the control device imperfection. During test UR1 ϑ varies up to 720°, and two complete rotations of principal strain rate axes are obtained.

The obtained stress-path is plotted in the deviatoric plane

$$\frac{\sigma_x - \sigma_y}{2} \div \sigma_{xy}$$

(Figure 12), from which it is evident that the imposed principal strain axes rotation involves a principal stress axes rotation. The relation between α_σ and $\alpha_{\dot{\varepsilon}}$ is plotted in Figure 13: an average 30° delay between the direction of principal stress and the direction of principal strain rate is found, even

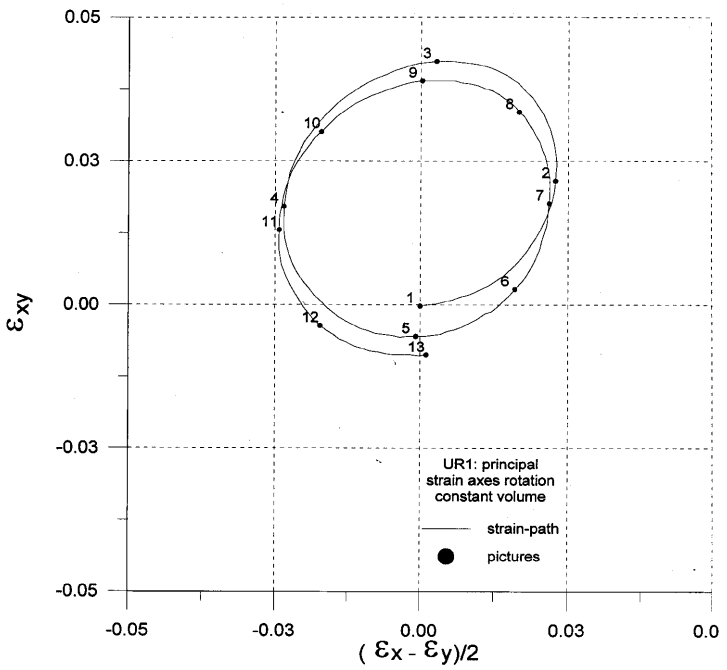

Figure 11. Test UR1: deviatoric strain-path

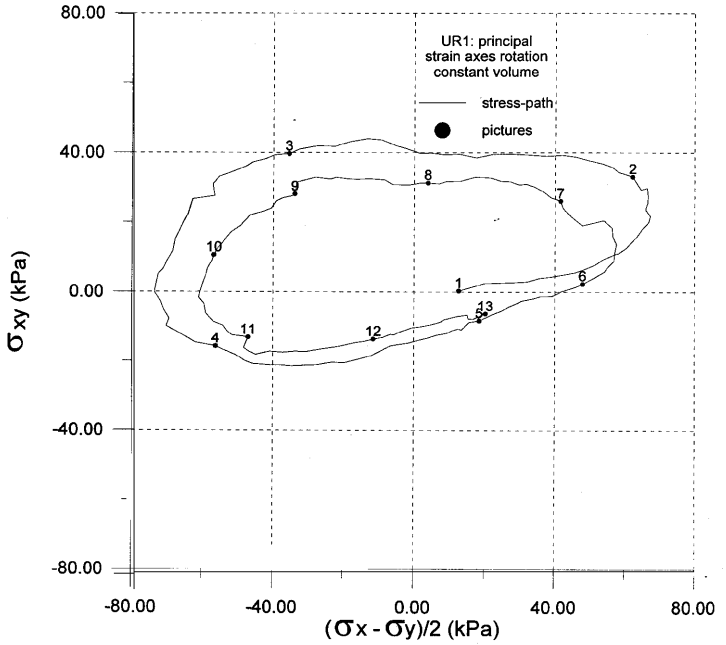

Figure 12. Test UR1: deviatoric stress-path

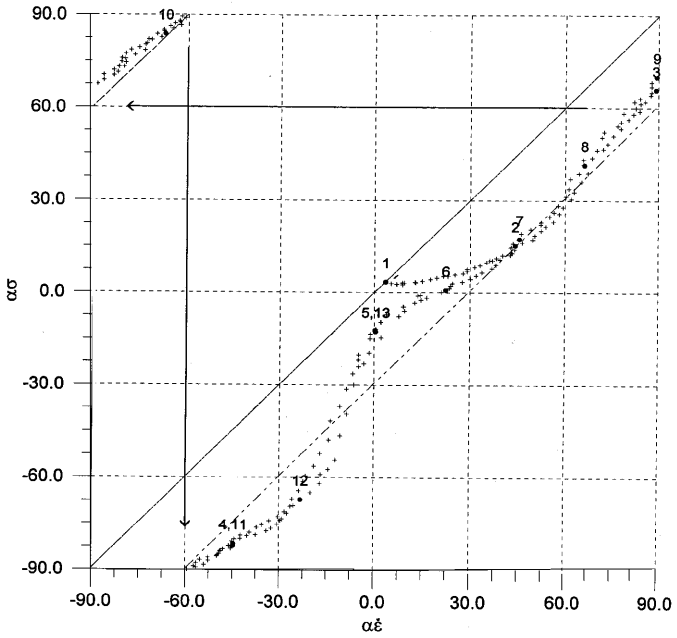

Figure 13. Test UR1: relation between compression rate direction, $\alpha_{\dot{\varepsilon}}$, and major principal stress direction, α_{σ}

if some deviations take place. Similar results were experimentally obtained by Matsuoka, Iwata and Sakakibara,[30] and Joer.[31]

4. CONTINUUM MECHANICS AND GRANULAR MATERIALS

4.1. Particle displacements

Our micromechanical measurements give the displacements of each roller centre. This displacement field may be compared with that which a homogeneous continuum would exhibit under the same boundary conditions. During a general load interval defined by two pictures, say i and j, under the boundary kinematics imposed by the loading device, the continuum mechanics stream lines of the displacement vector field have the form (see Appendix B):

$$x = C \cdot |y|^{\alpha/\rho} - \frac{\beta}{\alpha - \rho} \cdot y$$

where C is an integration constant and α, β and ρ depend on the specimen size at time t_i and t_j, regardless of the followed strain-path (homogeneous deformation is assumed). On the other hand, actual displacements are measured for each roller comparing its centre position on picture negatives i and j.

A typical result is plotted in Figure 14, in which arrows represent measured roller centre displacements while solid lines are continuum mechanics stream lines (CVCH1 vertical compression, pictures 1 to 4). On average, rollers move in the directions prescribed by continuum mechanics, even if some local deviations are observable. The analysis of this latest point is strictly related to strain localization and the corresponding micromechanical features will be detailed in Section 4.5.

The actual displacement distribution during shear test UDUG1 (Figure 15(top)) can be conveniently analysed displaying, at different stages of the test, the profiles of horizontal components of

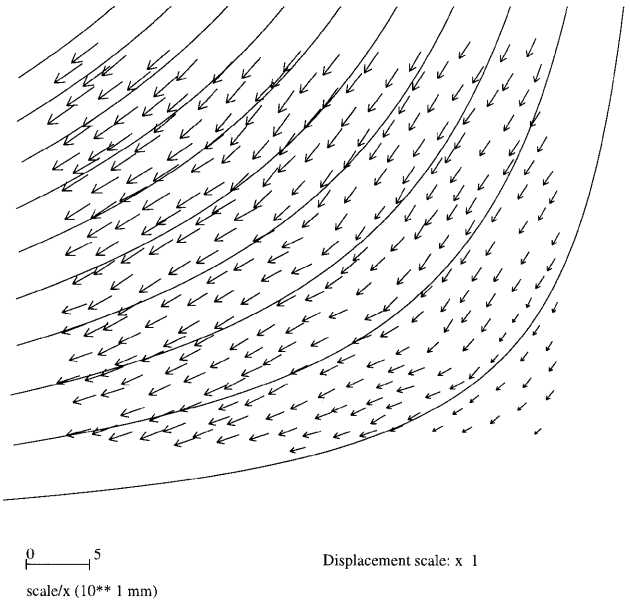

Figure 14. Roller displacement field (arrows) and continuum mechanics streamlines (solid lines); test CVCH1, vertical compression (pictures 1 to 4)

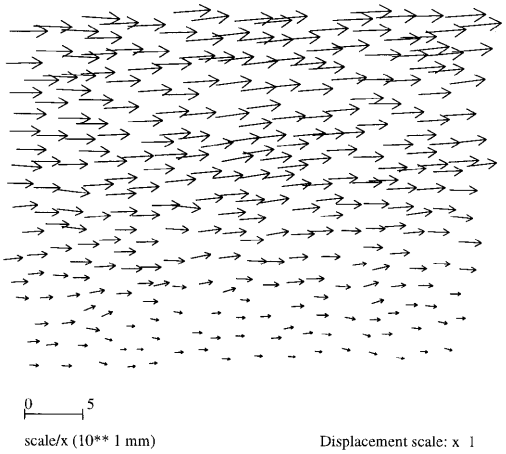

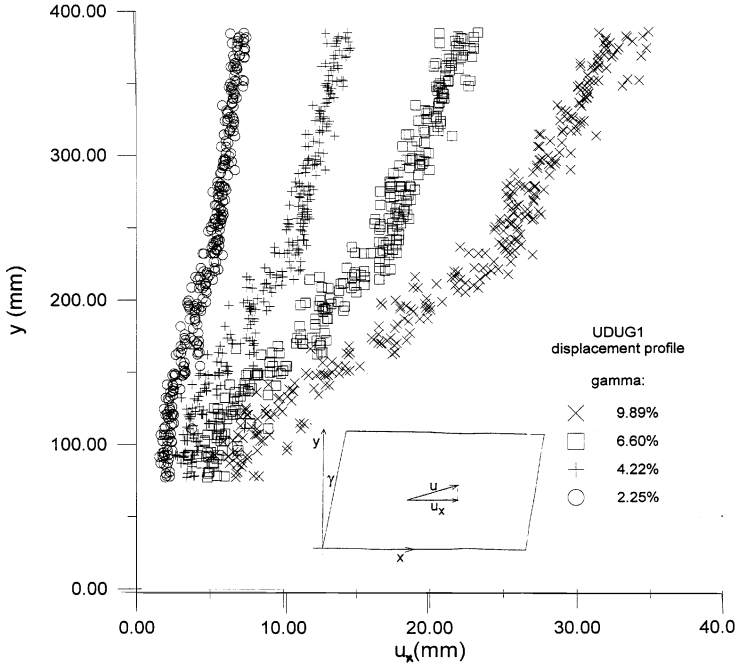

Figure 15. Test UDUG, right-shear part: (top) roller displacements field (pictures 1 to 5); (bottom) profiles of roller horizontal displacements

roller displacement u_x versus y (Figure 15(bottom)). During shear tests the corresponding continuum mechanics profile is a straight line $u_x = k \cdot y$ passing from the axes origin. As the test proceeds, experimental data become more and more scattered, and the bottom part of the specimen is characterized by larger values of the displacements vertical gradient; the corresponding local deformation features will be shown in Section 4.5.1.

Some further information can be derived from test UR1, in which principal deformation axes are continuously rotated. In such a test the direction of incremental compression continuously changes and an interval can be selected such that cumulative strains, for instance, result in a vertical compression (pictures 2 to 4 of Figure 16). The corresponding roller displacements lie along the stream lines pattern again with good precision. Therefore it seems that roller displacements are also not path-dependent and are only determined by the initial and final position of the plates.

These results are not surprising: in a dense 2D-material specimen, particles are strictly constrained, and their possibility to migrate within the specimen is quite low; therefore the overall displacement field remains close to continuum mechanics predictions.

4.2. Particle rotations

Under the hypothesis of continuum mechanics, the loading machine kinematics requires that the specimen rigid rotation, ω_s (anti-symmetric part of the displacement gradient), is equal to one half of the lateral plate rotation, γ. On the other hand, microrotations are evaluated comparing the orientation of each roller diameter on two different picture negatives. Results can be either directly plotted on a rotation chart or analysed from a statistical standpoint.

Particle rotations growth during testing can be studied by evaluating the mean value, $\bar{\omega}$, and the standard deviation $\bar{\sigma}$ of the rotation distribution. Results for the compression test CHCV1 are presented Figure 17. First of all, it is interesting to note that the mean value keeps close to 0°, which is the specimen rigid rotation during compression, and the small drift from zero that is accumulated during loading is partially recovered when unloading. On the other hand, the standard deviation becomes larger and larger during loading phases and only slightly decreases during unloading.

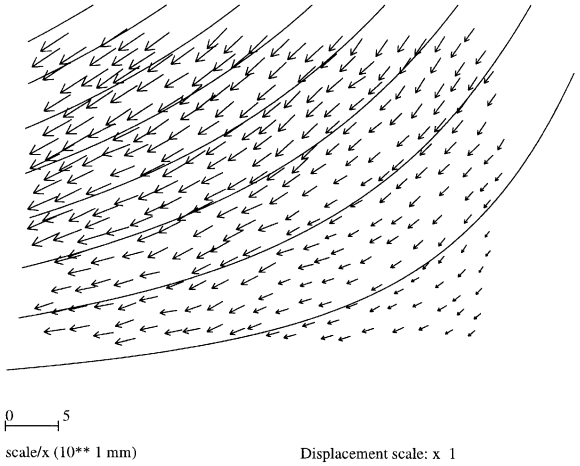

Figure 16. Roller displacement field (arrows) and continuum mechanics streamlines: test UR1, pictures 2 to 4

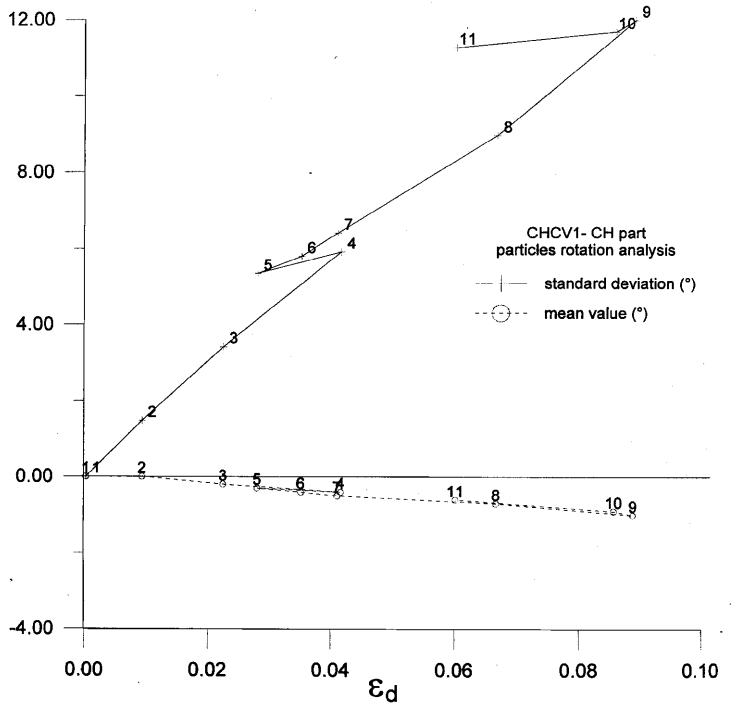

Figure 17. Mean value and standard deviation of rotation distribution: test CHCV1, horizontal compression

Results of test CHCD1, in which compression is followed by shear under constant confining pressure, are presented in Figure 18. In this case, the mean value of particle rotations increases during shear, and keeps close to the rigid rotation of the specimen, even if the standard deviation is continuously increasing and reaches quite large values.

The common tendency of the standard deviation to become larger and larger means that the rotation distribution within the specimen is more and more disordered as the test goes on. In fact, the material we employed is composed of circular rods for which a certain rotational freedom is granted, even in a dense 2D material. For this reason, it seems interesting to underline the link between rotations mean value and specimen rigid rotation, which means that average rotational behaviour of particles is still ruled by the applied boundary conditions. The described close relation between $\bar{\omega}$ and ω_s does not hold if results of test UR1, in which continuous axes rotation is performed, are analysed: in this case only the general trends of $\bar{\omega}$ and ω_s are similar, but the mean value of particle rotations increasingly drifts from the rigid rotation of the specimen (Figure 19).

4.3. Strain tensor definition

In continuum mechanics the strain tensor is defined as:

$$\varepsilon_{ij} = \frac{1}{2}(u_{i,j} + u_{j,k}),$$

in which $u_i = u_i(x, y)$ is the displacement vector field and $u_{i,j}$ its gradient. The difficulty with micromechanics of granular materials is that the function $u_i(x, y)$ is not continuous and the previous

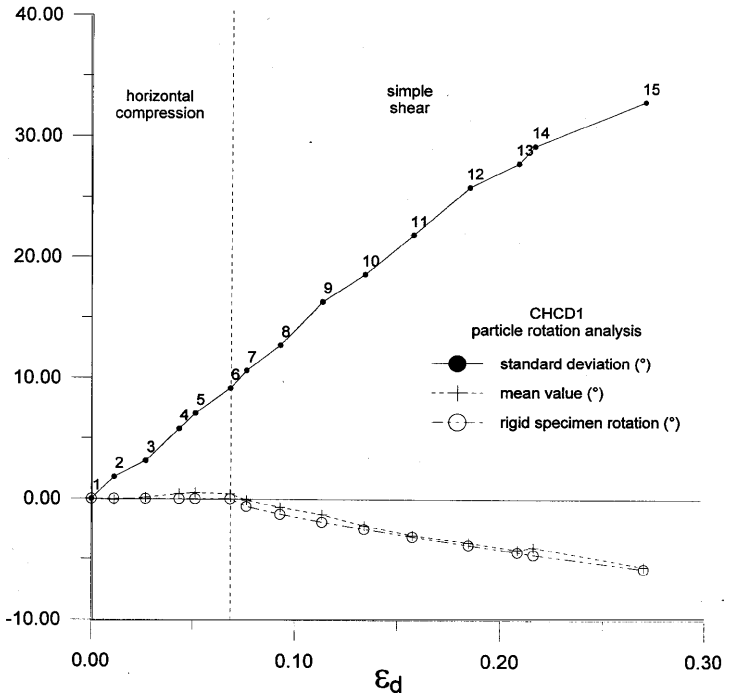

Figure 18. Mean value and standard deviation of rotation distribution: test CHCD1

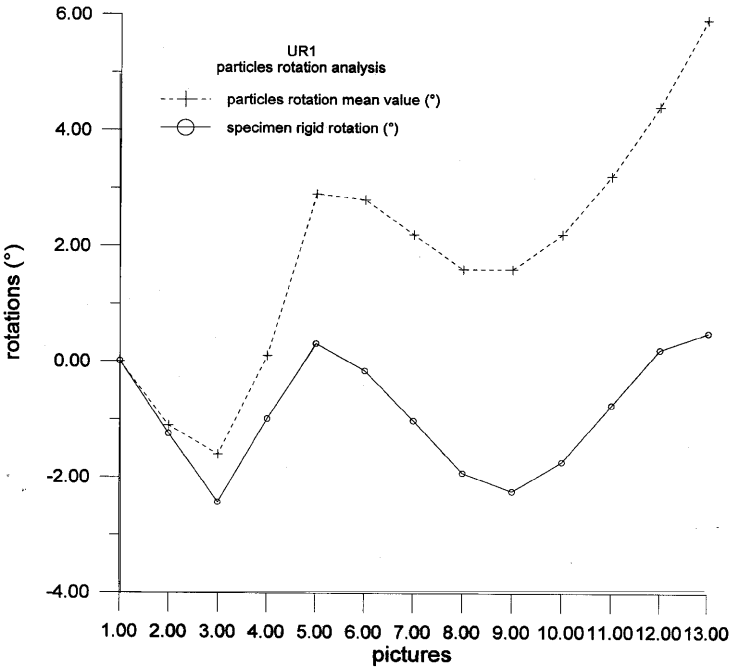

Figure 19. Rigid specimen rotation and mean roller rotation versus picture number, test UR1

definition must be adapted. Two homogenization approaches, that will be discussed in the following paragraphs, may be used:

1. Definition of a mean displacement for each roller and extension on the whole volume (surface in 2D). If particles are considered as rigid bodies, the displacements mean value over each roller volume is its geometrical centre displacement.
2. Definition of an equivalent deformation by use of internal work. In this case the relative displacements of contact points must be considered.

4.3.1. Approach (1): relative displacements of rollers. In continuum mechanics, the displacement gradient mean value, $\bar{u}_{i,j}$, can be defined over a surface, S, as:

$$\bar{u}_{i,j} = \frac{1}{S}\int_s u_{i,j}\mathrm{d}S$$

and applying Gauss's theorem:

$$\bar{u}_{i,j} = \frac{1}{L}\int_L u_i n_j \mathrm{d}L$$

where L is the contour of the considered surface and n_j the unit normal to the contour (Figure 20). Following an approach proposed by Cundall, Descher and Strack,[2] we may define a homogenized strain tensor based on this formula: as displacements measured at the centres of rollers corresponds to the rollers mean displacement, we choose as L a polygonal line joining the centres of particles defining the considered surface contour. Moreover, the hypothesis that the variation of displacement components u_i is linear along the segment joining roller centres is added. It is interesting to note that roller rotations are neglected in this approach. Once $\bar{u}_{i,j}$ is evaluated on the surface, it can be used to define local strains applying the same formula as used for macrostrains:

$$(\varepsilon_{ij})_{\mathrm{micro}} = \tfrac{1}{2}(\bar{u}_{i,j} + \bar{u}_{j,i})$$

The smallest surface on which the average is performed is defined for each roller on the basis of a Voronoi tesselation: the corresponding local strains are particularly useful for the study of strain localization, that will be detailed in Section 4.5.

4.3.2. Approach (2): relative displacements of contact points. Another attempt to define strain tensor from microkinematics can be based on energetic considerations and the use of a stress tensor definition from contact forces.[12]

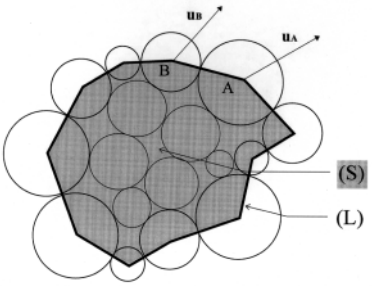

Figure 20. Averaging domain (S) with contour line (L) for microderived strain determination

First, the mean incremental work in volume V is written as:

$$W = \bar{\sigma}_{ij} \cdot \bar{u}_{i,j} = \frac{1}{V} \sum_{c=1}^{N} F_i^c \cdot u_i^c$$

where N is the number of contacts in volume V, u_i^c is the relative displacement of contact points, and F_i^c is the corresponding contact factor. Then, the classical definition of macrostress from contact forces is introduced:

$$\bar{\sigma}_{ij} = \frac{1}{V} \sum_{c=1}^{N} F_i^c \cdot l_j^c$$

where l_j^c is the branch vector, i.e., the vector joining the centres of the two particles in contact. The incremental work may be rewritten in the following way:

$$W = \frac{1}{V} \sum_{c} F_i^c \cdot l_j^c . \frac{l_j^c \cdot u_c^i}{\|\mathbf{l}^c\|^2} \approx \left(\frac{1}{V} \sum_{c} F_i^c \cdot l_j^c . \right) . \left(\frac{1}{N} \sum_{c} \frac{l_j^c \cdot u_i^c}{\|\mathbf{l}^c\|^2} \right)$$

where: $\|\mathbf{l}\|^2 = l_k^c \, . \, l_k^c$. The second equality in the previous expression, often referred to as Hill's condition, is questionable. Nevertheless, by comparison of the three previous relations we deduce the following expression for the mean displacements gradient:

$$\bar{u}_{i,j} = \frac{1}{N} \sum_{n=1}^{N} u_i^n \cdot \frac{l_j^n}{\|\mathbf{l}_n\|^2}$$

where the summation is extended to all contacts lying within the surface defining the considered volume. Then local strain ε_{ij} is deduced by taking the symmetric part of $\bar{u}_{i,j}$. It is necessary to note that in this definition the mean gradient appears as a summation of tensorial products $\mathbf{l} \otimes \mathbf{u}$, which is slightly different from the formulation proposed by Satake and Tobita.[12]

4.3.3. Evaluation of proposed definitions. To test these two different approaches to accuracy, we will compare microdefined strains to actual macrostrains applied at the loading device boundaries. As an example, we present results obtained from microkinematics homogenization during a compression test (Figure 21). The microderived strain tensor is calculated, following the two described procedures, taking into account the whole sample (300 rollers, about 1 200 contacts). While strains calculated from the first approach are close enough to the corresponding macrostrains, the second approach is not satisfactory, as microderived strains are quite different from strains applied at the boundaries. Therefore, in the following, we will always use microstrains derived from roller displacements (first approach).

4.4. Definition of elementary representative volume

In this section, we will focus our interest on the dependence of calculated microstrains on the size of the domain in which the average operation is performed, i.e., on the influence of the number of rollers considered to definee $\bar{u}_{i,j}$. If we trace, for each roller, a general calculated strain component (ε_{yy} in Figure 22) versus the area of the surface used to define the averaging procedure, we discover that the strain component values are initially very scattered and then quite rapidly converge to a common value which is close to the corresponding macrostrain component. For this reason, the domain over which a size increase does not affect, in a significant way, the calculated average strains, can be considered as the elementary representative surface (volume) of the discontinuous material. The size of the representative volume is found to be about ten times larger than the biggest roller

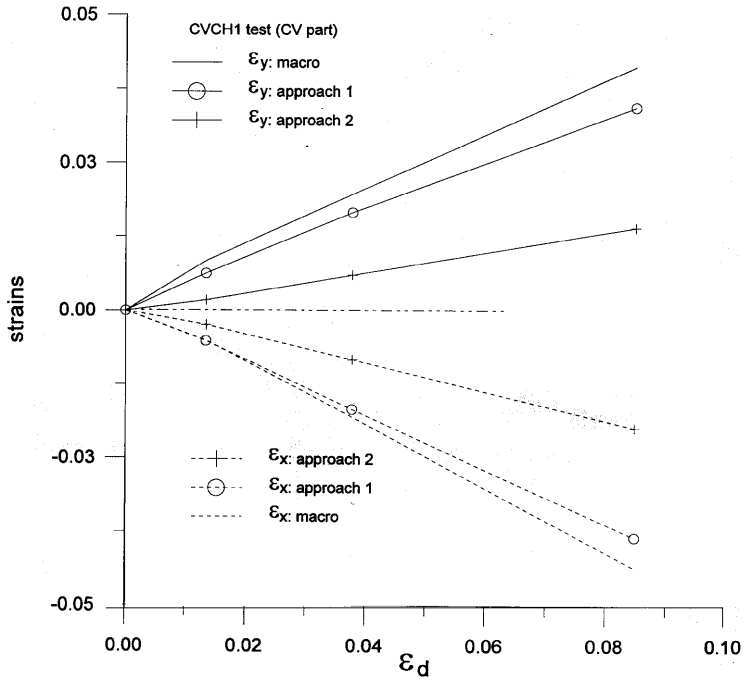

Figure 21. Comparison between boundary strains and microderived strains for CVCH1 vertical compression

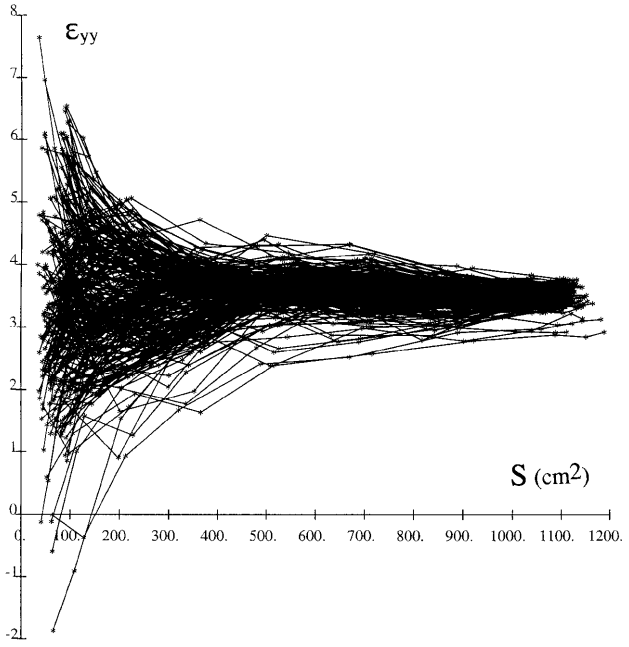

Figure 22. Microstrain ε_y versus averaging domain surface: test CVCH1, vertical compression (boundary strain ε_y 4%)

diameter: this result confirms evidence that other authors found by means of numerical analysis via DEM based codes.

4.5. Local strain and strain localization

A local strain in the vicinity of each roller may be defined in the following way:

- Neighbours of each roller are identified by a 2D-Voronoi tessellation. By this way we obtain the closest line (L) (Figure 20) surrounding the roller under consideration.
- The approach described in Section 4.3.1 (approach 1) is used to estimate local strain ε_{ij}.

According to the previous results, these local strains do not have any meaning at the macroscale but they may characterize micromechanisms of deformation, and in particular they may be used to analyse the phenomenon of strain localization. For this purpose, the spatial evolution of microstrain distribution within the specimen is analysed, plotting local deformation charts corresponding to different pictures taken during testing. Any component of a local strain tensor can be used but the deviatoric intensity of the local strain tensor (maximum shear: $e = \varepsilon_I - \varepsilon_{II}$ where $\varepsilon_I > \varepsilon_{II}$ are the principal values of ε_{ij}), is considered as the most suitable variable to describe strain localization. As an example, we show results from test CVCH1, in which a vertical compression followed by unloading and by a horizontal compression is performed. At the end of the vertical compression (pictures 3 to 4, Figure 23(top)), the local deviatoric strains are particularly intense in a zone which defines a band, whose inclination to horizontal is about 50°. When unloading, the same band is still active, and seems more defined than during loading (pictures 4 to 5, Figure 23(middle)). As the load is reversed, the band first disappears and then develops with a new inclination of about 30° to horizontal (pictures 8 to 10, Figure 23(bottom)). The principal strain field presents the same pattern of the shear strains above. As an example, we show the plot corresponding to the end of compression load (pictures 3 to 4, Figure 24): local principal strains are particularly intense in a band; moreover, principal strain directions are on the average oriented along the x and y axes, which are principal directions of macrostrains. Outside the band, principal strains are smaller, and their orientation seems more disordered.

4.5.1. Local deformation features. In this section we will detail the micromechanical features which are related to microstrain localization. First of all, it is interesting to note that local strains are larger where the corresponding displacement field deviates from that predicted by continuum mechanics. We will first analyse the results of test UDUG1, whose displacement profile was plotted in Figure 15(bottom). The corresponding local strain chart (Figure 25) is characterized by larger values in the bottom part of the specimen, where the vertical gradient of horizontal displacements is larger (Figure 15(bottom)).

In an analogous way, the displacement field (Figure 26(top)) corresponding to the end of the CVCH1 compression load is characterized by a discontinuity, which coincides with the large strain zone in Figure 23(top).

Corresponding to microstrain localization, local kinematics is characterized by the occurrence of large particle rotations. In fact, with reference to the end of CVCH1 compression, particle rotations (Figure 26(middle)) are particularly intense along the displacement field discontinuity line, where microstrains are localised.

4.5.2. Localization band thickness. In the previous section, we have shown that corresponding to strain localization bands, microkinematics is characterized by intensification of particle rotations. The transverse thickness of the zone where microstrains are localized contains three or four roller, and

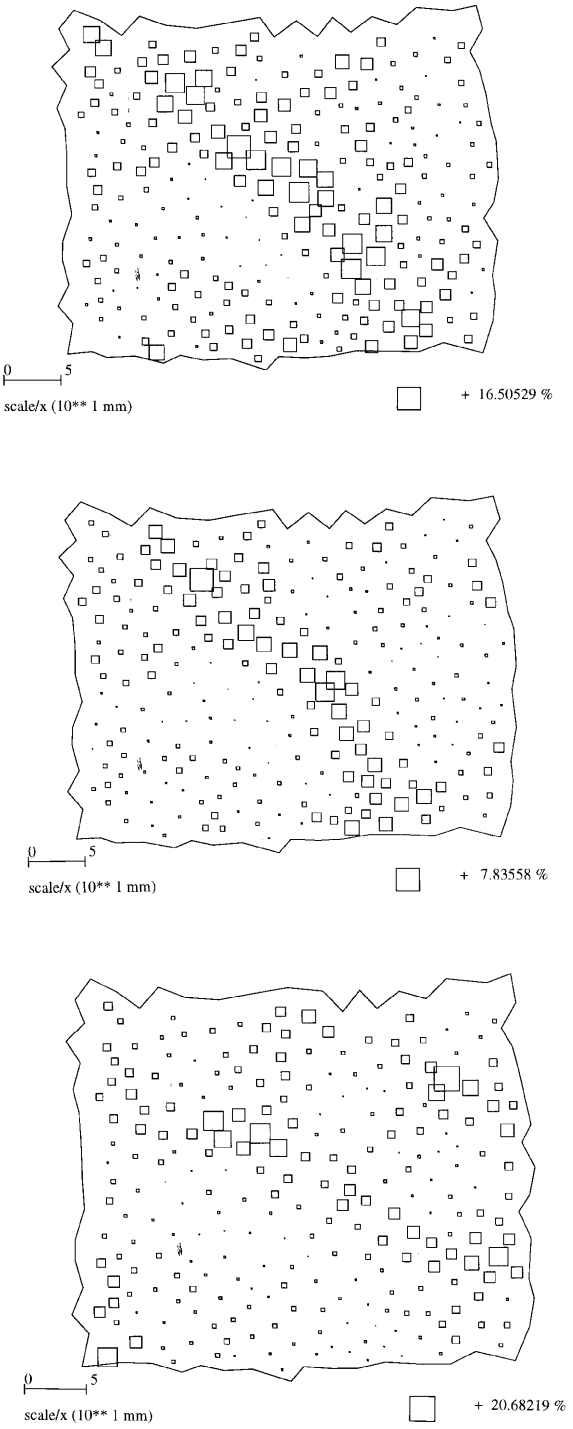

Figure 23. Deviatoric strain chart: test CVCH1; (top) end of vertical compression, pictures 3 to 4; (middle) unloading, pictures 4 to 5; (bottom) end of horizontal compression, pictures 8 to 10

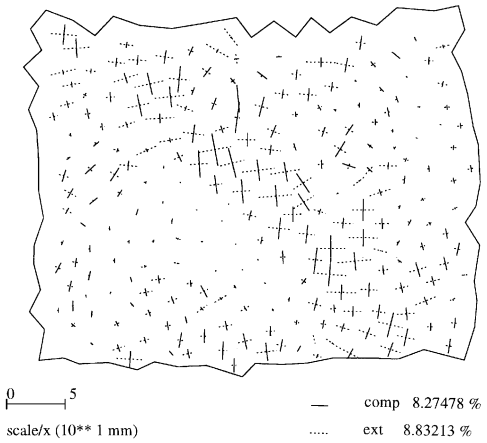

Figure 24. Principal strain field: test CVCH1, end of vertical compression, pictures 3 to 4

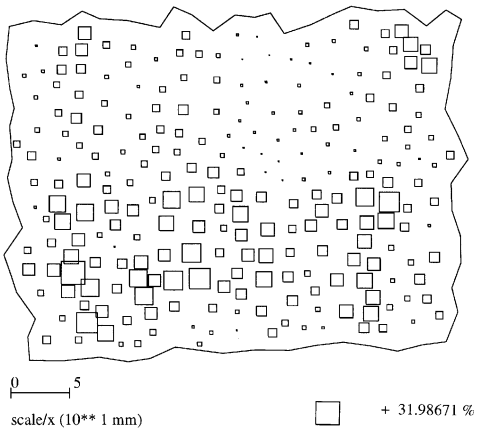

Figure 25. Deviatoric strain chart: test UDUG1, pictures 1 to 5

rotations are localized in a narrow band, containing one or two rollers: if local kinematics is considered, the localization band tends to collapse in a line, which is closely related to the fact that the displacement field is characterized by a well defined discontinuity line. Anyway, the previously defined elementary representative volume is not contained in the band thickness. Therefore, the use of continuum mechanics to describe the mechanical behaviour inside the shear band seems questionable, even if the obtained results are certainly influenced by the 2D nature of our specimens.

5. CONTACT EVOLUTION AND STRUCTURE ANISOTROPY

One of the reasons that makes a granular material exhibit a complex macrobehaviour is that its internal structure continuously changes during loading: this phenomenon, which is commonly defined as induced anisotropy, is strictly related to the discontinuous nature of the material, which involves an intrinsic weakness; in particular, the fact that contacts cannot resist in tension allows large structure rearrangements.

5.1. Definition of structural variables

The specimen structure is characterized by the geometry of contacts and voids. In general, the variables used to analyse contacts are the co-ordination number *Nc*, defined as number of contacts over number of particles, and the angular distribution of contacts.

Experimentally, we detect a contact between two particles if the distance between their centres does not exceed by a fixed threshold the sum of respective radii. The introduction of a tolerance is intended to avoid errors due to the manual digitization of photograph negatives and to the fact that actual rod's cross-section is not exactly circular; the tolerance value we adopted is fixed at 0.5 mm.

To make possible a stastistical study, contacts are grouped in eighteen 10° wide ranges, on the basis of their normal orientation versus horizontal x-axis. The specimen structure can be represented in a histogram where the number of contacts $N(\theta_i)$ belonging to each range is plotted versus the mean class orientation, $\theta_i (i = 1, 18$ and $\sum_i N(\theta_i) = N_0$ is the total number of contacts). To perform an analytical study, actual histograms are often replaced by a second-order Fourier approximation, written in the form:

$$N(\theta) = m \cdot \{1 + d \cdot \cos[2(\theta - \theta_0)]\}$$

with $d > 0$ and

$$m = \frac{N_0}{\pi},$$

which can efficiently interpolate distributions having only one maximum over the interval $-90^\circ \leqslant \theta \leqslant +90^\circ$. In an equivalent way (see Appendix C), we can admit the existence of a symmetric tensor **F** which verifies the relation:

$$N(\theta) = \mathbf{n}^{\mathrm{T}} \cdot \mathbf{F} \cdot \mathbf{n}$$

with $\mathbf{n}^{\mathrm{T}} = [\cos(\theta) \sin(\theta)]$; the major principal direction of **F** is θ_0.

As an example, we show histograms of $N(\theta)$ corresponding to the beginning (picture 1) and to the end (picture 4) of CVCH1 compression load. It is evident that the initial specimen structure is not isotropic (Figure 27(a)), due to the random specimen construction under gravity field. It is important to remark that initial anisotropy is difficult to erase, and affects the specimen structure all over the following test (Figure 27(b)). Moreover, since the contact distribution has two maximum points, the second-order Fourier approximation cannot fit experimental data.

Therefore, the *evolution of the specimen structure* during a load increment, defined by two pictures, say i and j, is analysed introducing the variable:

$$S(\theta) = \frac{N_j(\theta)}{N_i(\theta)} = 1 + \frac{\Delta N(\theta)}{N_i(\theta)}$$

where $N_j(\theta)$ and $N_i(\theta)$ are the number of contacts detected on picture i and j respectively, and $\Delta N(\theta) = N_j(\theta) - N_i(\theta)$. The meaning of this variable can be explained in the following way: during

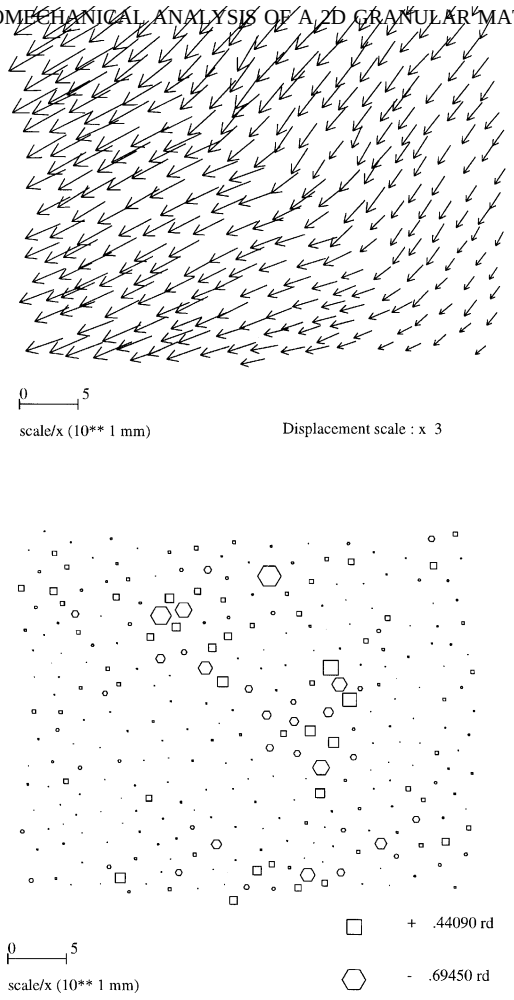

Figure 26. Test CVCH1, end of vertical compression (pictures 3 to 4); (top) displacement field; (bottom) rotation chart

deformation from picture i to j, there are contacts which are maintained, while others are lost or gained. Let us consider a general range orientation, $\bar{\theta}$. If $S(\bar{\theta}) < 1$, there are more lost contacts than gained ones in the considered range; if $S(\bar{\theta}) < 1$ the reverse conclusion may be made; if $S(\bar{\theta}) = 1$, the number of contacts within the considered range is stationary. The histogram of $S(\theta)$ corresponding to CVCH1 compression load (pictures 1 to 4) is plotted in Figure 27(c). It shows that structure evolution, represented by $S(\theta)$, is not influenced by the initial anisotropy and the proposed second-order Fourier approximation of $S(\theta)$ is quite acceptable. It is important to underline the fact that this result does not depend on the particular load increment considered, and has most general validity. For instance, in Figure 28 we show structure evolution during UDUG1 test (right-shear part, pictures 1 to 5). In this case, $S(\theta) = 1$ for $\theta = 0^\circ$ and $\theta = -80^\circ$. Under constant volume shear, zero-extension lines, defined in continuum mechanics by the condition $\varepsilon_n = 0 (\varepsilon_n = n_i \cdot \varepsilon_{ij} \cdot n_j)$, lie along x and y axes.

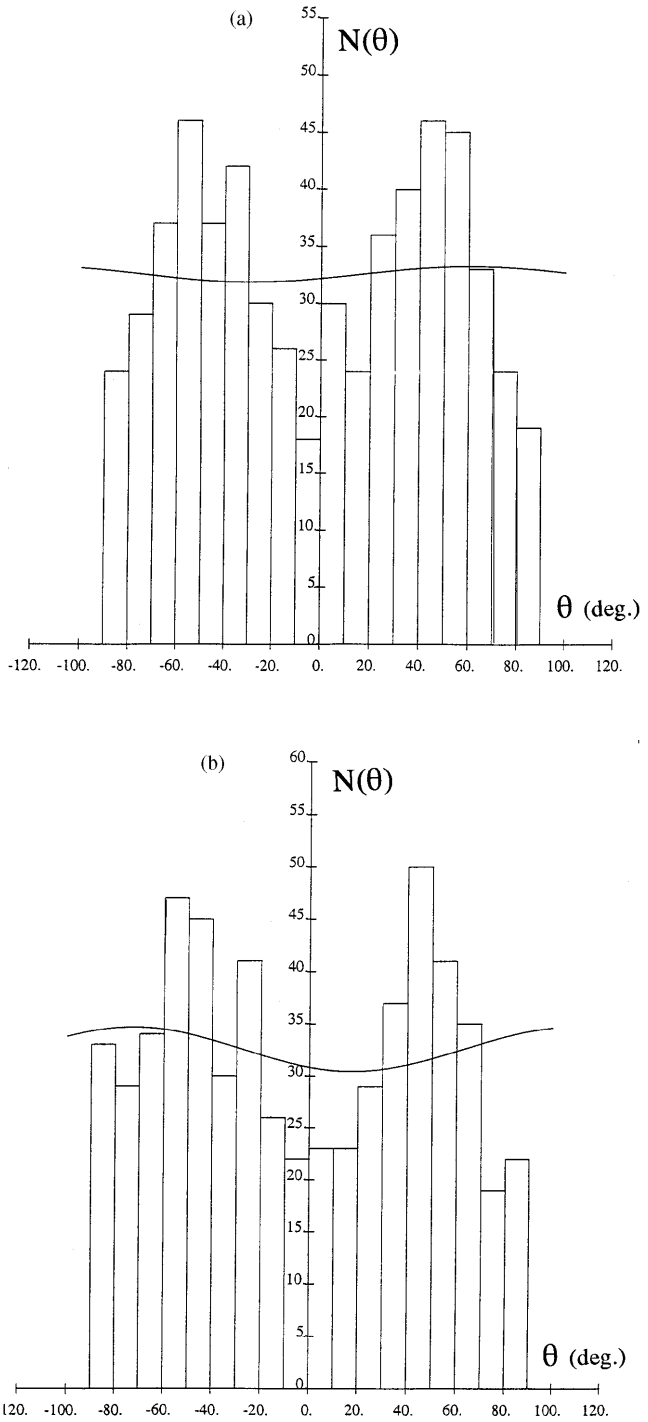

Figure 27. Contact orientation histogram, test CVCH1: (a) initial structure (picture 1); (b) structure at the end of vertical compression (picture 4); (c) structure evolution during vertical compression (pictures 1 to 4)

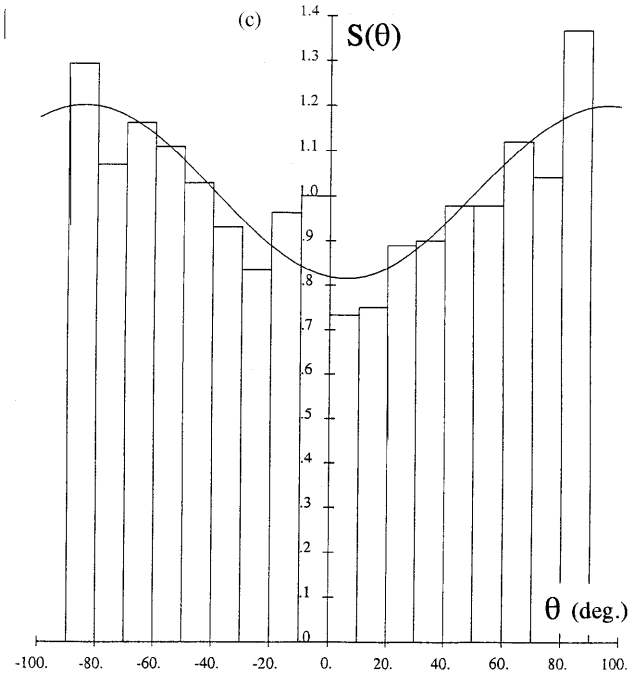

Figure 27. (*continued*)

For this reason, one could conclude that the contact number is stationary in the direction of zero-extension lines.

As long as the Fourier approximation is good, we can use parameters m, d and θ_0 to describe fabric evolution. In particular, m, which is the mean value of Fourier approximation, is related to the variation of the co-ordination number Nc (in all our tests m is close to 1); d is the width of Fourier approximation normalized to m, and will be called *rearrangement anisotropy*; θ_0 is the direction corresponding to the maximum contact gain, and will be called *rearrangement orientation*. Another consequence of the validity of the second-order Fourier approximation is that there exists a second-order symmetric tensor **A**, such that

$$S(\theta) = \mathbf{n}^{\mathrm{T}} \cdot \mathbf{A} \cdot \mathbf{n}$$

with θ_0 the major principal orientation of $\mathbf{A}$, $m = \frac{1}{2}\mathrm{tr}(\mathbf{A})$, and $m \cdot d$ equal to the intensity of the deviatoric part of **A**.

5.2. Internal structure evolution

In this section we will analyse the specimen fabric evolution under different loading conditions, and we will relate micromechanical results with the macro behaviour that was described in Section 3. Where not specified, we will always choose the initial specimen configuration (picture 1) as the reference one to define $S(\theta)$ and the corresponding parameters m, d and θ_0.

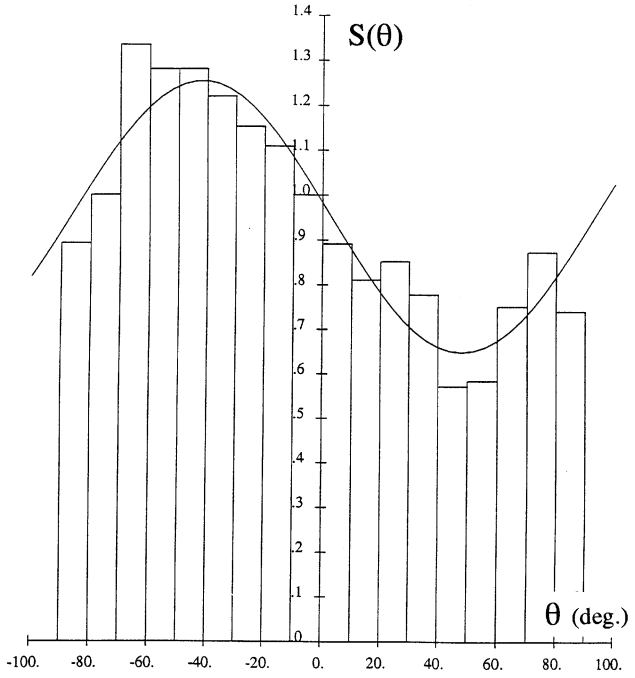

Figure 28. Structure evolution during test UDUG1 (right-shear part, pictures 1 to 5)

5.2.1. Influence of principal axes permutation on specimen fabric. For a general load increment, as usual defined by two pictures, *i* and *j*, boundary *compression direction* is defined by angle $\alpha_{\Delta\varepsilon}$ between the direction of major principal strain increment and the *x*-axis. Depending on load type $\alpha_{\Delta\varepsilon}$ is equal to: 90° or 0°, for vertical ($\Delta\varepsilon_y > 0$) and horizontal ($\Delta\varepsilon_x < 0$) compressions respectively; $+45^\circ$ or -45° for right-shear ($\Delta\gamma > 0$) and left shear ($\Delta\gamma < 0$) under constant volume, respectively.

We will first consider the CHCV1 test, whose macro results are described in Section 3.2.1 (Figure 4): at the end of the horizontal compression load (CH part, pictures 1 to 9) the specimen structure has undergone an evolution which mostly involves horizontal contact gain and vertical contact loss (Figure 29(a)). The structure has an anisotropic evolution, and rearrangement orientation coincides with compression direction. The same trend is found if we compare the structure at the end of unload with the initial one (Figure 29(b)), pictures 1 to 11). This means that anisotropy, which has developed during loading, is not recovered when unloading. This fact puts in close relation fabric anisotropy with macrostrains, since plastic strains are found at the end of unload. Therefore, when the load is reversed, and the specimen is subjected to vertical compression, the specimen structure has initially a lack of contacts in the new direction of load. This result explains the fact that the initial stiffness (Figure 4) is lower than during the first load and slightly increases, as compression goes on, when contacts are progressively gained back in the vertical direction. In fact, at the end of vertical compression, fabric evolution is anisotropic with the maximum gain of contacts in the vertical direction (pictures 1 to 16, Figure 29(c).

These results can be conveniently summarized by plotting the evolution of parameters d and θ_0 (Figure 30). Rearrangement anisotropy (parameter d) increases and decreases with the modulus of

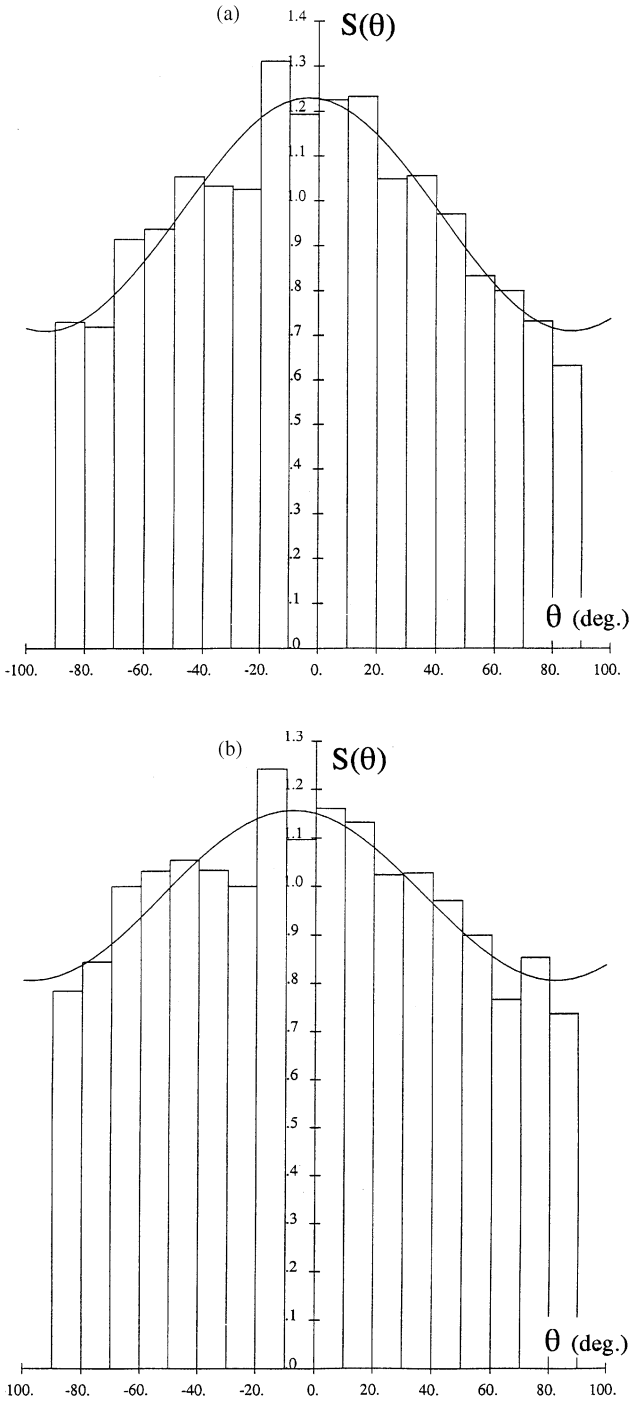

Figure 29. Structure evolution during test CHCV1: (a) horizontal compression end (pictures 1 to 9); (b) unloading end ($\sigma_y = \sigma_x$, pictures 1 to 11); (c) vertical compression end (pictures 1 to 16)

$\varepsilon_x - \varepsilon_y$, which corresponds to deviatoric strain, and rearrangement orientation (parameter θ_0), passes from $\sim 0^\circ$ to $\sim 90^\circ$ as cumulative strains pass from horizontal to vertical compression.

The same trend is found analysing the UVUH1 and UDUG1 tests, whose macrobehaviour was described in Section 3.2. In particular, during the UVUH1 compression part (pictures 1 to 5), as rearrangement anisotropy grows, rearrangement orientation keeps close to the vertical direction (Figure 31). Structure anisotropy developed during the load phase is not completely recovered at the end of unloading ($\sigma_x = \sigma_y$, picture 6): for this reason, the interval between pictures 6 and 8 is characterized by the fact that rearrangement orientation is still vertical, while the load is applied in horizontal compression ($\Delta\varepsilon_x > 0, \sigma_x > \sigma_y$). This means that, even if the macrodensity is equal to the initial one, the horizontal contact number has decreased with respect to the initial configuration. As a consequence, the specimen macrobehaviour is qualitatively similar to that of a dense sand during the first compression, and similar to that of a medium-dense sand at the beginning of the second one, as described in Section 3.2.1. It is interesting to remember that the specimen stiffness seems to increase as soon as the condition $\varepsilon_x - \varepsilon_y > 0$ is met, i.e., when rearrangement orientation and compression rate direction coincide.

In an analogous way, we can give a micromechanical interpretation of the UDUG1 macroresults, that were described in Section 3.2.2 (Figure 7). First of all, it seems interesting to point out that the structure evolution is really closely linked to boundary deviatoric strain, which is equal to the modulus of applied γ (Figure 32(top)), and an almost reversible behaviour is found when shear strain is reversed; in particular, when $\gamma = 0$ rearrangement anisotropy is about 0. During the same test, rearrangement orientation (Figure 32(bottom)) is really close to -45° (from pictures 2 to 7, $\gamma > 0$) and to $+45^\circ$ (from pictures 9 to 13, $\gamma < 0$), which are compression directions under right and left-shear respectively. The macro specimen response to the imposed strain-path was characterized

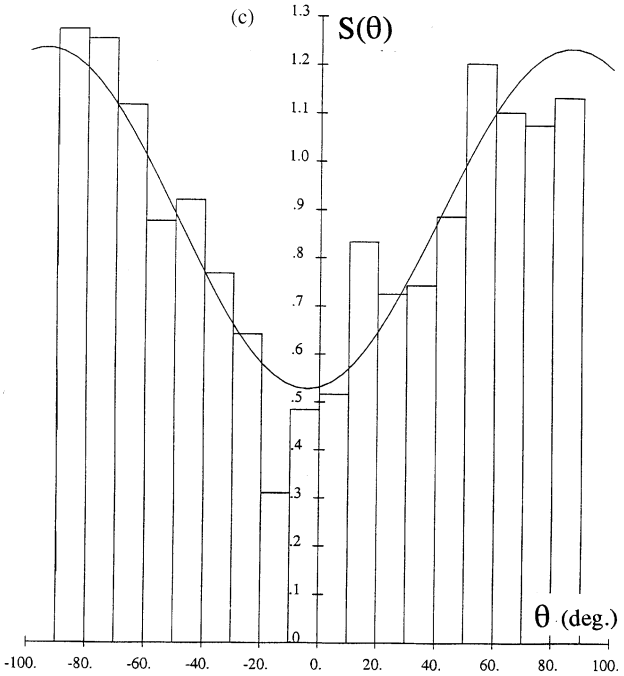

Figure 29. (*continued*)

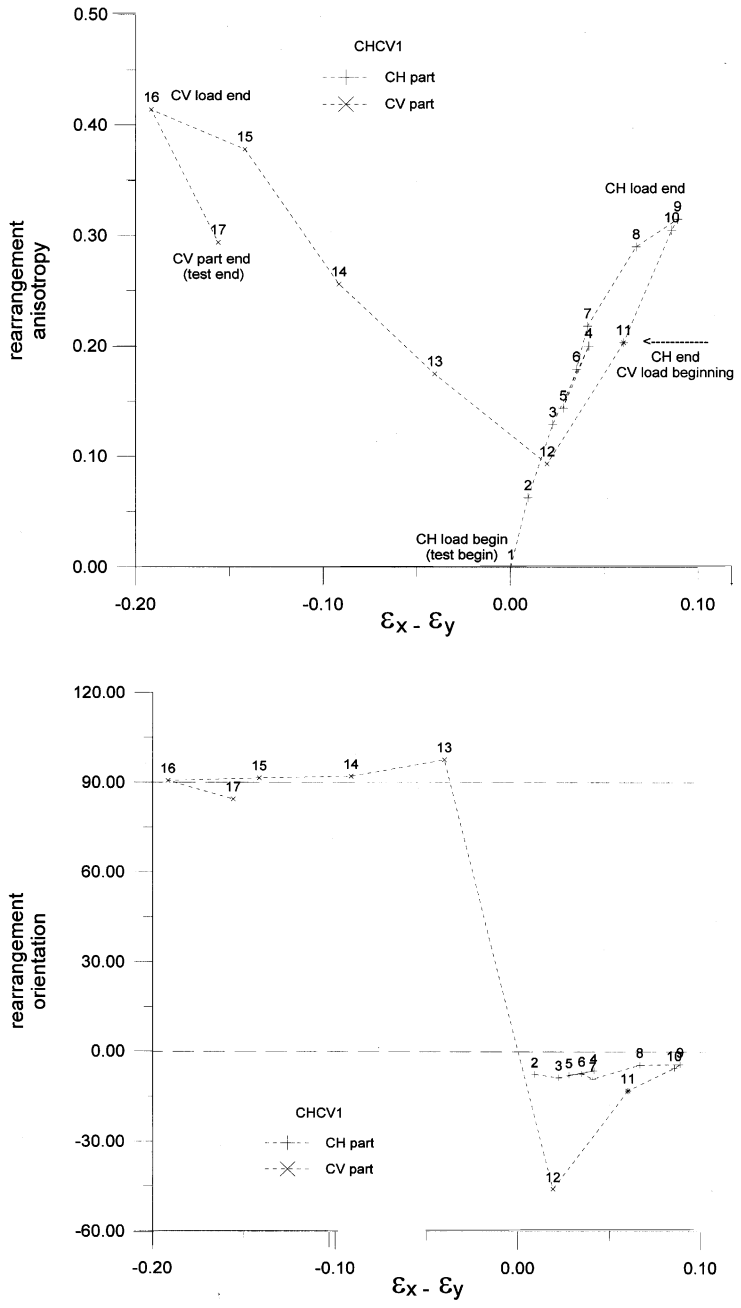

Figure 30. Structure evolution during test CHCV1: (top) rearrangement anisotropy: parameter d versus $\varepsilon_x - \varepsilon_y$; (bottom) rearrangement orientation: parameter θ_0 versus $\varepsilon_x - \varepsilon_y$

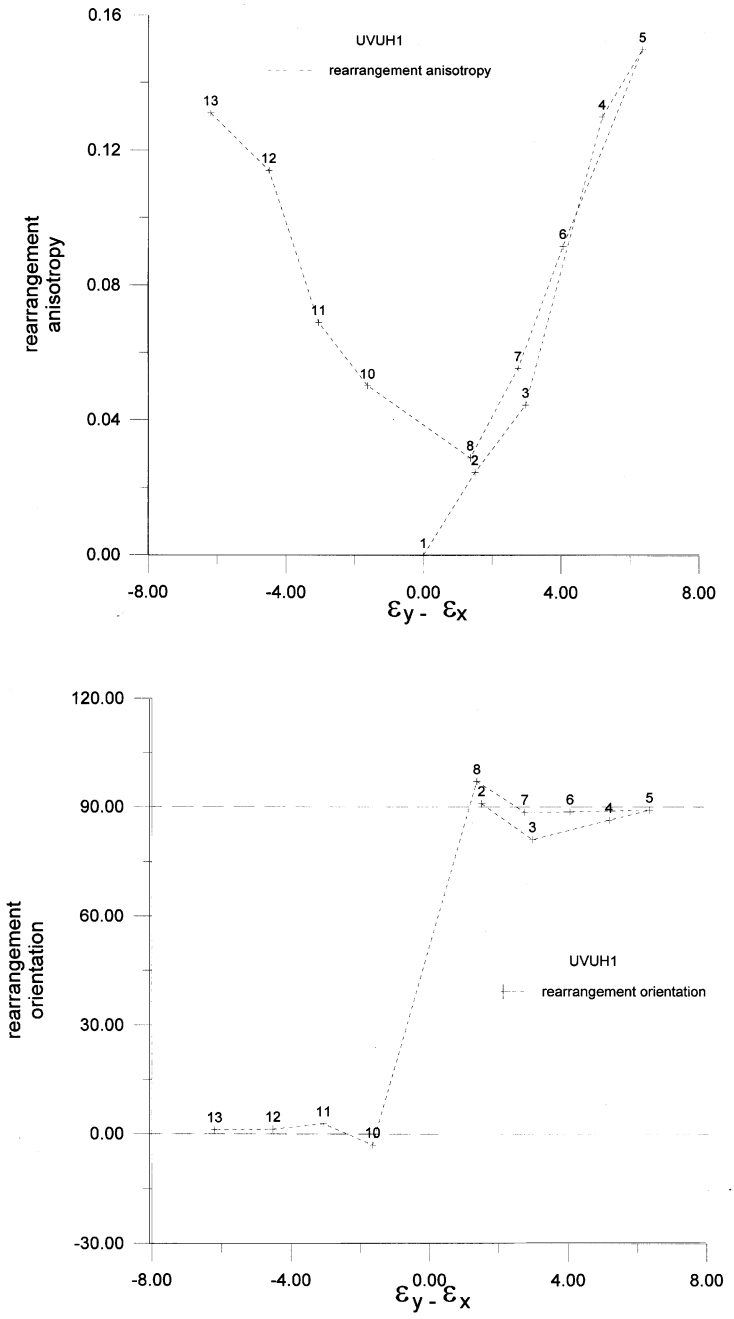

Figure 31. Structure evolution during test UVUH1: (top) rearrangement anisotropy: parameter d versus $\varepsilon_y - \varepsilon_x$; (bottom) rearrangement orientation: parameter θ_0 versus $\varepsilon_y - \varepsilon_x$

(Figure 7(top)) by three load phases, beginning at points corresponding to pictures 1, 6 and 12. The fact that the specimen stiffness is higher during the first load is easily interpreted analysing structure evolution: in fact, while the first load is carried by a structure that we consider isotropic, corresponding to points 6 and 12, internal structure is oriented in the direction opposite to that of compression rate, which means that a lack of contacts, with respect to initial structure, is found in the direction of load.

In conclusion, we have shown that under constant volume conditions, rearrangement anisotropy is really closely linked to deviatoric strains, and structure evolution presents a reversible behaviour when strains are reversed. This is partially due to the fact that during a constant volume test, which is fully strain-controlled, particle kinematics is strictly constrained in dense 2D specimens.

5.2.2. Anisotropy and structural instability. In this section we will give a micromechanical interpretation of the results of the CHCH1 test (Section 3.3.1). In particular we will link roller instabilities with the evolution of structure anisotropy. If we plot structure rearrangement anisotropy versus deviatoric macrostrain (Figure 33), we discover that specimen structure becomes more and more anisotropic as the test goes on, except for intervals from pictures 4 to 5 and from 13 to 14. As previously described, two points (A and B on Figure 8) were experimentally characterized by local instabilities of a group of rollers. It may be interesting to note that these points coincide with the intervals where rearrangement anisotropy decreases. In particular, at point B, where a volumetric collapse takes place and the stress control is lost for a while, the decrease in structure anisotropy is evident.

5.2.3. Structure rearrangement under continuous principal strain axes rotation. In previous analyses, principal directions of strain, strain increment, stress, and structure rearrangement (tensor **A** principal directions), respectively defined by angles α_ε, $\alpha_{\Delta\varepsilon}$, α_σ and θ_0, were coincident (0° or 90° for compression tests, $+45^\circ$ or -45° for the constant volume shear test). On the other hand, during test UR1 α_ε, $\alpha_{\Delta\varepsilon}$ and α_σ are no longer the same (Figures 11 and 13). To analyse structure rearrangement, we compare the two orientations $\alpha_{\Delta\varepsilon}$ and θ_0, both calculated for the load increment between two successive pictures, say i and $i+1$. Figure 34 shows very clearly that we have $\alpha_{\Delta\varepsilon} \cong \theta_0$. This experimental result indicates that tensors **A** and $\Delta\varepsilon$ have the same principal axes, and we can write the tensorial relation:

$$\mathbf{A} = a \cdot \mathbf{I} + b \cdot \Delta\varepsilon, \text{ (2D condition)}$$

or

$$S(\theta) = \mathbf{n}^{\mathrm{T}} \cdot \mathbf{A} \cdot \mathbf{n} = a + b \cdot \Delta\varepsilon_n(\theta)$$

where $\Delta\varepsilon_n(\theta)$ is the incremental strain in the direction defined by θ, and **I** is the unit tensor. In principle a and b may be scalar functions of $\Delta\varepsilon$, i.e. $a = a(\Delta\varepsilon)$ and $b = b(\Delta\varepsilon)$. In particular, a must verify the condition $a(\mathbf{0}) = 1$ ($S(\theta) \equiv 1$ if no deformation is applied) and we can rewrite the previous relation as: $\mathbf{A}' = \mathbf{A} - \mathbf{I} = a'\mathbf{I} + b.\Delta\varepsilon$, with $a'(\mathbf{0}) = 0$. This new tensor is associated with the variation of $N(\theta)$ by the following relation;

$$\frac{\Delta N(\theta)}{N(\theta)} = \mathbf{n}^{\mathrm{T}} \cdot \mathbf{A}' \cdot \mathbf{n} = a' + b \cdot \Delta\varepsilon_n(\theta)$$

We have previously seen that $\Delta N(\theta) = 0$ closely corresponds to $\Delta\varepsilon_n(\theta) = 0$ (contact number is stationary along zero-extension lines). As a consequence, we may admit $a' = 0$. Moreover, as a first

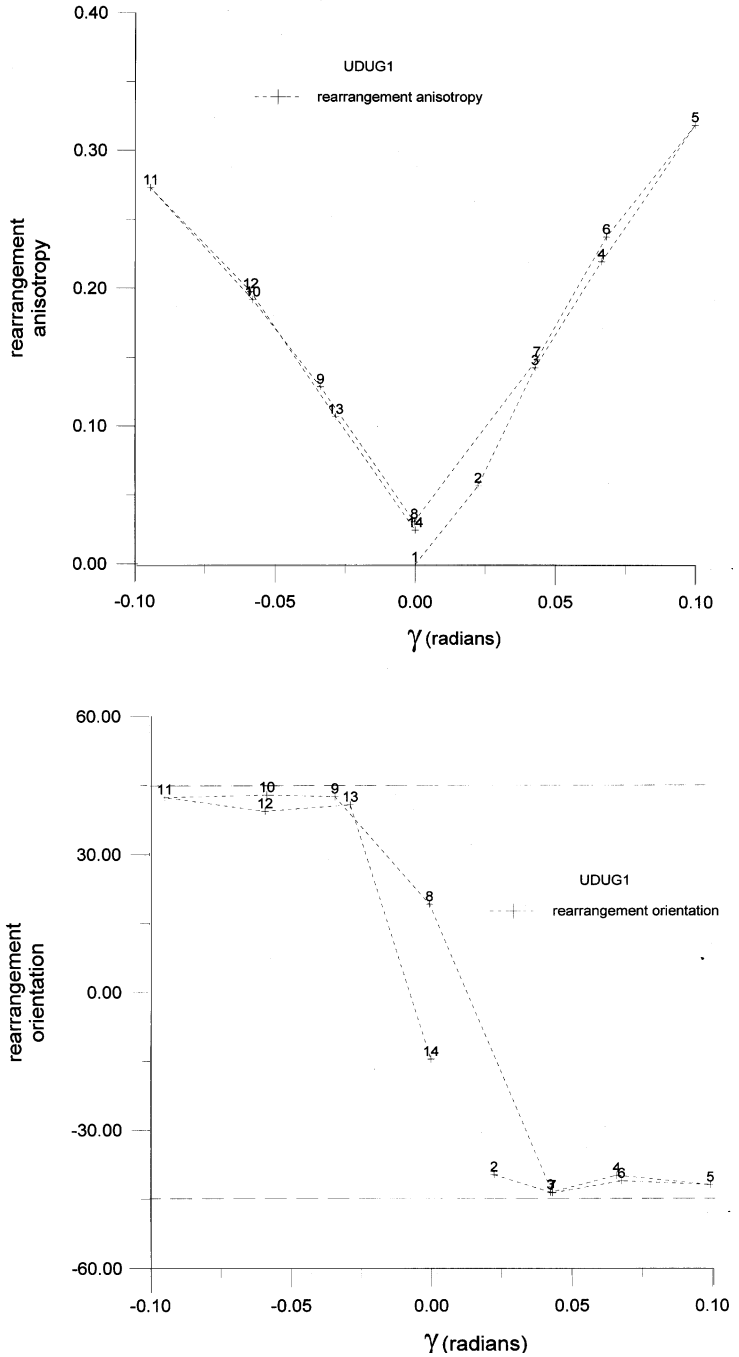

Figure 32. Structure evolution during test UDUG1: (top) rearrangement anisotropy: parameter d versus γ ; (bottom) rearrangement orientation: parameter θ_0 versus γ

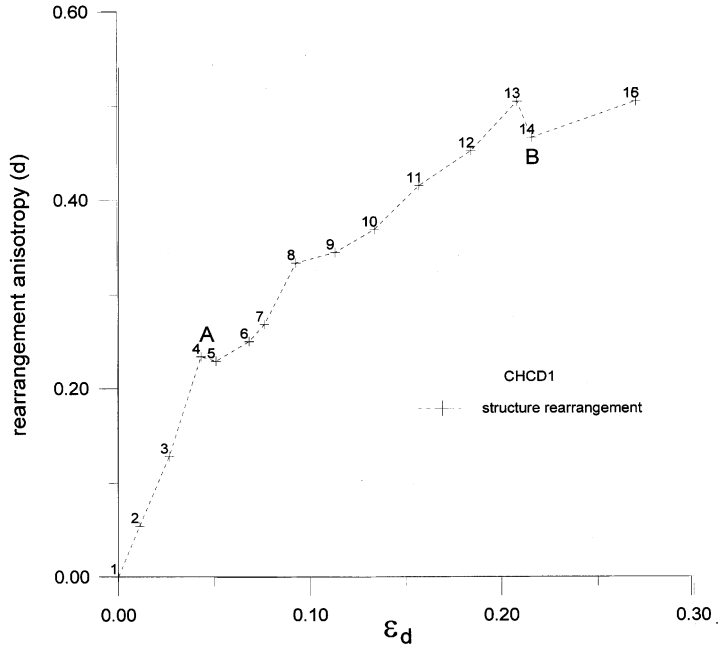

Figure 33. Structure evolution during test CHCD1: rearrangement anisotropy: parameter *d* versus deviatoric strain

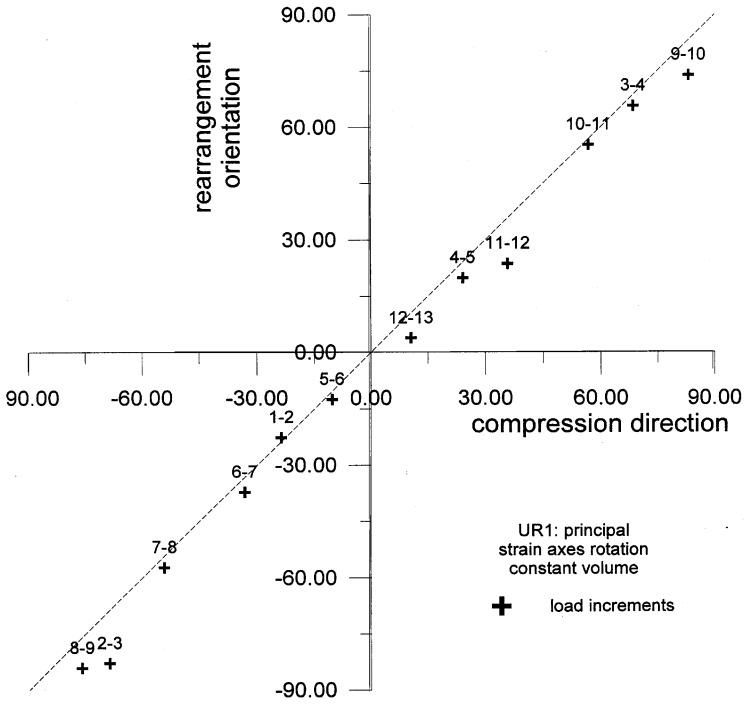

Figure 34. Structure evolution under continuous principal axes rotation (test UR1): relation between compression direction, $\alpha_{\Delta\varepsilon}$, and rearrangement orientation, θ_0

approximation, we suppose b to be constant during loading. In this case, tensors $\mathbf{A}'$ and $\Delta\varepsilon$ are proportional, and by integration we have:

$$\frac{\Delta N(\theta)}{N_0(\theta)} \approx \ln\frac{N(\theta)}{N_0(\theta)} = b \cdot \varepsilon_n(\theta) = b \cdot \left\{\frac{\varepsilon_I + \varepsilon_{II}}{2} + \frac{\varepsilon_I - \varepsilon_{II}}{2}\cos[2(\theta - \theta_0)]\right\}$$

This relation takes into account results obtained in the previous section, concerned with the rearrangement parameter d. In fact, for constant volume tests

$$\frac{\varepsilon_I + \varepsilon_{II}}{2} = 0,$$

and d is proportional to deviatoric strain

$$\frac{\varepsilon_I - \varepsilon_{II}}{2}$$

(see Figures 31(a) and 32(a).

We have shown that structure anisotropy is closely dependent on deformations applied at the specimen boundary. Anyway, certain care is necessary before extending this result to the modelling of real granular materials, since particle kinematics, on which structure rearrangement is based, is strictly constrained in dense 2D packages, especially under constant volume conditions.

6. CONCLUSIONS

With our shear apparatus $1\gamma 2\varepsilon$ we are able to apply general 2D-deformation conditions; in particular, principal axes rotation may be produced. Several tests have been performed on Schneebeli material specimens (circular wooden rods, with three different diameters) and the results are analysed in terms of macroscopic behaviour and micromechanical kinematics.

First of all, we have verified that the macroscopic behaviour of this 2D-material is qualitatively similar to that of real granular materials, such as sands, performing different loading paths such as compression, shear and constant volume tests. In particular, induced anisotropy must be invoked to explain the observed behaviour.

Secondly, micromechanical kinematic variables such as roller displacement field and roller rotations, are compared with continuum mechanics predictions for a fictitious homogeneous material subjected to the same boundary conditions. Our conclusions are that the roller centres displacement field is close to continuum mechanics predictions, except along lines where localization occurs. Roller rotations are very scattered with standard deviation increasing with strain but, for compression and shear tests at least, their mean value is very close to the rigid specimen rotation deduced from continuum mechanics. In tests with continuous principal axes rotation this correlation is not so good: only the general evolution may be compared.

For each roller, a local strain tensor is defined, taking into account the displacements of neighbour rollers. By displaying the local shear intensity chart, the shear band mechanism of deformation is clearly demonstrated. The thickness of the detected band is only two or three rollers, far less than the elementary representative volume for use of continuum mechanics (about 10 rollers, in our case).

Finally, the contact orientation evolution is analysed. Because of the contacts lost and gained during deformation of the specimen, a rearrangement of the material structure takes place, which may be modelled by a second-order symmetric tensor, $\mathbf{A}'$, which gives the variation of contact number in a material direction $\mathbf{n}$. As a first approximation, $\mathbf{A}'$ may be considered proportional to the incremental strain tensor $\Delta\varepsilon$. This simplifying hypothesis explains quite well the evolution of induced anisotropy in the sample.

In conclusion, it is necessary to underline that the obtained micromechanical information needs careful evaluation before an extension to the modelling of a real granular material can be proposed. If the use of an analogous 2D-material composed of wooden rollers allows relatively simple micro-kinematic measurements, the observed behaviour is certainly influenced by the 2D nature of the specimens, as often remarked on in the text. Moreover, the use of wooden rollers does not allow one to access the microforces world. In our work, this restriction will be overcome by testing, with the shear device $1\gamma 2\varepsilon$, specimens composed of photoelastic rollers, and by means of numerical simulations based on the distinct elements method. In this case, numerical specimens can be generated identical to the laboratory ones, using data obtained from pictures digitization.

APPENDIX A. MEASUREMENT OF INTERGRANULAR FRICTION ANGLE

The intergranular friction angle Φ was directly measured using the experimental technique described in Figure 35.

The two rollers A and B are fixed and support roller C which is loaded by the two weights P_1 and P_2. Initially, P_1 and P_2 are equal and rod C is obviously in equilibrium. By increasing P_2, a limit equilibrium is reached and rod C rotates and slides at contact points with rods A and B. At this time, the equilibrium equation gives the following relation:

$$\sin 2\Phi = 2 \,.\, \frac{P_2 - P_1}{P_2 + P_1} \,.\, \frac{L}{R} \,.\, \cos\alpha$$

This relation is valid if $\alpha > \Phi$ (both contacts are maintained when the sliding condition is reached). Many tests, performed with different α and P_1 values, allow an estimation of $\Phi = 28^\circ(\pm 2^\circ)$ for our wooden rollers with smooth surfaces.

APPENDIX B. CONTINUUM MECHANICS STREAMLINES DERIVATION FROM DISPLACEMENT VECTOR FIELD

Let us consider two configurations i and j of our shear apparatus, defined by the boundary conditions $(L_{1i}, L_{2i}, \gamma_i)$ and $(L_{1j}, L_{2j}, \gamma_j)$, and let us suppose that these two configurations define an homogenous deformation for a 2D-continuum. Then displacement $\mathbf{u}(x, y)$ is a linear function of the co-ordinates (x, y) in the configuration i. Under the special kinematics imposed by our apparatus it may be shown that the two components of $\mathbf{u}(x, y)$ are:

$$u_x = \alpha \,.\, x + \beta \,.\, y$$
$$u_y = \rho \,.\, y$$

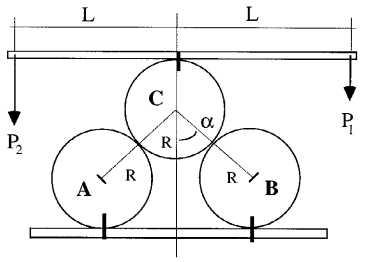

Figure 35. Measurement of intergranular friction angle

where the following notation applies:

$$\alpha = \frac{L_{1j} - L_{1i}}{L_{1i}}$$
$$\beta = \frac{L_{2j}.\sin\gamma_j}{L_{2i}.\cos\gamma_i} - \frac{L_{1j}.\sin\gamma_i}{L_{1i}.\cos\gamma_i}$$
$$\rho = \frac{L_{2j}.\cos\gamma_j}{L_{2i}.\cos\gamma_i} - 1$$

The streamlines of this vector field are obtained by integration of the following differential equation:

$$\frac{\mathrm{d}x}{u_x(x,y)} = \frac{\mathrm{d}y}{u_y(x,y)}$$

whose general solution may be written as:

$$x = C|y|^{\alpha/\rho} - \frac{\beta.y}{\alpha - \rho}$$

where C is an arbitrary constant. If we plot these curves, the tangent at point (x, y) gives the direction of the displacement vector in a continuum which deforms homogeneously from configuration i to configuration j.

APPENDIX C. RELATION BETWEEN SECOND-ORDER FOURIER EXPANSION AND SYMMETRIC SECOND-ORDER TENSOR

Let us suppose that a scalar quantity is expressed by a second-order Fourier expansion:

$$N(\theta) = a + b \cdot \cos 2(\theta - \theta_0)$$

This expression may be developed in a quadratic form of the two variables $x = \cos\theta$ and $y = \sin\theta$. Then let us consider the unit vector $\mathbf{n}(\cos\theta, \sin\theta)$ and the symmetric tensor associated with this quadratic form, $N(\theta)$ may be rewritten as:

$$N(\theta) = \mathbf{n}^{\mathrm{T}} \cdot \mathbf{A} \cdot \mathbf{n} \quad \text{or} \quad N(\theta) = n_i \,.\, A_{ij} \,.\, n_j$$

with the following components A_{ij} of tensor $\mathbf{A}$:

$$A_{11} = a + b \cdot \cos 2\theta_0 \quad q_{22} = a - b \cdot \cos 2\theta_0 \quad A_{12} = A_{21} = b \cdot \sin 2\theta_0$$

REFERENCES

1. A. Drescher and G. de Josselin de Jong, 'Photoelastic verification of a mechanical model for the flow of a granular material', *J. Mech. Phys. Solids*, **20**, 337–351 (1972).
2. P. A. Cundall, A. Descher and O. D. L. Strack, 'Numerical experiments on granular assemblies; measurement and observations', *IUTAM Conference on Deformation and failure of granular materials*, eds. P. A. Vermeer and H. J. Luger, Delft, Balkema, pp. 355–370, 1982.
3. J. P. Bardet and J. Proubet, 'A numerical investigation of the structure of persistent shear bands in granular media', *Geotechnique*, **41**, 599–613 (1991).
4. J. Christoffersen, M. M. Mehrabadi and S. Nemat-Nasser, 'A micromechanical description of granular material behaviour', *J. of Applied Mechanics*, **48**, 339–344 (1981).
5. M. M. Mehrabadi, S. Nemat-Nasser and M. Oda, 'On statistical description of stress and fabric in granular materials', *Int. j. numer anal. methods geomech.*, **6**, 95–108 (1982).

6. D. Caillerie, 'Evolution quasitatique d'un milieu granulaire: loi incrémentale par homogénéisation', in *Des Géomatériaux aux Ouvrages*, eds. C. Petit, G. Pijaudier Cabot and J. M. Reynouard, Hermes, pp. 53–80, 1995.
7. D. Caillerie, 'Tenseur des contraintes dans un milieu granulair', *Rapport d'activité Greco*, 771–775 (1991).
8. R. Hill, 'Elastic properties of reinforced solids: some theoretical principles', *J. Mech. Phys. Solids*, **11**, 357–372 (1963).
9. B. Cambou, 'From global to local variables in granular materials', *Proc. Powders & Grains 93*, ed. Thornton, Balkema pp. 75–86, 1993.
10. B. Cambou, P. Dubujet, F. Emeeriault and F. Sidoroff, 'Homogenization of granular materials', *Eur. J. Mech. A. Solids*, **14**(2), 255–276 (1995).
11. M. Oda, S. Nemat-Nasser and M. M. Mehrabadi, 'A statistical study of fabric in a random assembly of spherical granules', *Int j. num. anal. methods in geomech.*, **6**, 77–94 (1982).
12. M. Satake and Y. Tobita, 'Mechanics of granular materials, XII° ICMSMFE, Rio de Janeiro, 1989.
13. C. Thornton and G. Sun, 'Triaxial compression of 3D polydisperse systems of spheres', *Proc. Powders & Grains 93*, ed. Thornton, Balkema, pp. 129–134, 1993.
14. L. Rothenburg and R. J. Bathurst, 'Analytical study of induced anisotropy in idealized granular materials', *Geotechnique*, **39**(4), 601–614 (1989).
15. L. Rothenburg and R. J. Bathurst, 'Micromechanical features of granular assemblies with planar elliptical particles', *Geotechnique*, **42**(1), 79–95 (1992).
16. H. Matsuoka and S. Yamamoto, 'A microscopic study on shear mechanism of granular materials by DEM and experiments', *Proc. Powders & Grains 93*, ed. Thornton, Balkema, pp. 155–160, 1993.
17. M. Mahboubi, 'Contribution à l'étude micromécanique des matériaux granulaires: modélisation des forces de contacts et simulation numérique', Ph.D. Thesis, Ecole Centrale de Lyon, 1995.
18. F. Calvetti, A. Lugan and R. Nova, 'Micromechanical analysis of a Schneebeli material specimen', *Proc. Numog V*, eds. G. N. Pande and S. Pietruszczak, Balkema, pp. 51–56, 1995.
19. B. Bornarel, 'Analyse numérique du comportement des matériaux granulaires', DEA report, Ecole centrale de Lyon, 1995.
20. Jl. Biarez and K. Wiendiek, 'Comparison qualitative entre l'anisotropie mécanique et l'anisotropie de structure des milieux pulvérulents', *C. R. Acad. Sci.*, **256**, 12–17 (1963).
21. M. Oda, J. Konishi and S. Nemat-Nasser, 'Experimental micromechanical evaluation of the strength of granular materials: effects of particle rolling', in *Mechanics of Granular Materials, New Models and Constitutive Relations*, eds. J. T. Jenkins and M. Satake, Elsevier Science Publishers, pp. 21–30, 1983.
22. P. Dantu, 'Contribution à l'étude mécanique et géométrique des milieux pulvérulents', *Proc. 4th Int. Conf. Soils Mech. Found. Eng.*, London, pp. 144–148, 1957.
23. J. Konishi, M. Oda and S. Nemat-Nasser, 'Inherent anisotropy and shear strength of assembly of oval cross-sectional rods', *IUTAM Conference on Deformation and Failure of Granular Materials*, eds. P. A. Vermeer and J. J. Luger, Delft, Balkema, pp. 403–412, 1982.
24. H. G. B. Allersma, 'Photoelastic stress analysis and strains in simple shear', *IUTAM Conference on Deformation and Failure of Granular Materials*, eds. P. A. Vermeer and H. J. Luger, Delft, Balkema, pp. 345–353 (1982).
25. H. Joer, J. Lanier, J. Desrues and E. Flavigny, '$1\gamma 2\varepsilon$: a new shear apparatus to study the behavior of granular materials', *Geotech. Testing J.*, **15**(2), 129–137 (1992).
26. J. R. F. Arthur, K. S. Chua and T. Dunstan, 'Principal stress rotation: a missing parameter', *J. Geotech. Eng. Div. ASCE*, **106**(GT4), 419–433 (1980).
27. B. Cambou and J. Lanier, 'Induced anisotropy in cohesionless soils: experiments and modelling', *Computers and Geotechniques*, **6**, 291–311 (1988).
28. J. Lanier, C. di Prisco and R. Nova, 'Etude experimentale et analyse theorique de l'anisotropie induite du sable d'Hostun', *Rev. Française de Géotechnique*, **106**, 59–74 (1991).
29. D. M. Wood, A. Drescher and M. Budhu, 'On the determination of stress state in the simple shear apparatus', *Geotech. Testing J.*, **2**(4), 211–221 (1979).
30. J. Matsuoka, H. Iwata and K. Sakakibara, 'A constitutive model of sand and clay for evaluating the influence of rotation of the principal stress axes', *Proc. 2nd Int. Symp. on Num. Models in Geomech.*, eds. G. N. Pande and W. F. van Impe, Ghent, Jackson and Sons, pp. 67–78, 1986.
31. H. Joer, '$1\gamma 2\varepsilon$: une nouvelle machine de cisaillement pour l'étude du comportement des milieux granulaires', Ph.D. Thesis, Université J. Fourier, Grenoble, 1991.
32. K. Bagi 'On the definition of stress and strain in granular assemblies through the relation between micro- and macro-level characteristics', *Powders and Grains 93*, ed. Thornoton, Balkema, pp. 117–121, 1983.